N71-33302
NASA CR-119914

INVESTIGATION OF SCALING CHARACTERISTICS FOR DEFINING DESIGN ENVIRONMENTS DUE TO TRANSIENT GROUND WINDS AND NEAR-FIELD, NON-LINEAR ACOUSTIC FIELDS

Interim Technical Report

This research work was supported by
the National Aeronautics and Space Administration
George C. Marshall Space Flight Center
Contract NAS8-30159

The University of Alabama in Huntsville
Division of Graduate Programs and Research
Research Institute
P. O. Box 1247
Huntsville, Alabama 35807

May 1971

INVESTIGATION OF SCALING CHARACTERISTICS FOR DEFINING DESIGN ENVIRONMENTS DUE TO TRANSIENT GROUND WINDS AND NEAR-FIELD, NON-LINEAR ACOUSTIC FIELDS

Interim Technical Report

This research work was supported by
the National Aeronautics and Space Administration
George C. Marshall Space Flight Center
Contract NAS8-30159

The University of Alabama in Huntsville
Division of Graduate Programs and Research
Research Institute
P. O. Box 1247
Huntsville, Alabama 35807

May 1971

PREFACE

The second year efforts of the research project entitled "Investigation of Scaling Characteristics for Defining Design Environments due to Transient Ground Winds and Near-Field, Non-Linear Acoustic Fields", the NAS8-30159 Contract for the period from April 1970 to May 1971 are presented in two sections of this report.

The first section entitled "Experimental Investigation of Pressure Wave Propagation in a Pipe" presents a report on the experimental investigation of propagation phenomena of nonlinear pressure waves in an open-end pipe containing air at atmospheric conditions. An instrumentation system consisting primarily of a battery of hot-film anemometers was used for the measurements of temporal and spacial velocity profiles for various diaphragm burst pressures. In order to gain a better insight of the physical phenomena, a mathematical model was developed by assuming the flow process isentropic. Calculated results from the mathematical model were compared with the experimental data. The discrepancy between the theory and experiment demonstrates the degree of anisotropic nature of the flow process. This task has been carried out primarily by Manfred J. Loh under the principal investigator's technical direction.

The second section entitled "Experimental Investigation of Effects of Unsteady Flows on a Submerged Cylinder" reports briefly results of the investigation of unsteady flow phenomena about a submerged right circular cylinder in various unsteady flow conditions. A set of dimensionless parameters consisting of quantities pertinent to the unsteady flows is used to analyze pressure and force data which are presented in terms of local pressure coefficients, lift and drag coefficients versus instantaneous Reynolds number and nondimensional fluid displacement respectively. The measured drag coefficients were found to be comparable with the calculated ones from the pressure coefficients.

A variation of the hydrogen bubble technique was used in obtaining high speed movies of the unsteady flow phenomena about the circular cylinder. A sequence of photographs taken from these movies is presented which shows the development of the flow field around the cylinder at various times.

This task has been undertaken primarily by David J. Morrow under the technical direction of the principal investigator. A detailed and final report of this task will be submitted later upon completion of the M.S. Thesis by Mr. Morrow.

These two tasks of the project were supported by staff members of the Fluid Dynamics Laboratory, Instrumentation Services Laboratory, Computer Laboratory, and the Machine Shop of The University of Alabama in Huntsville.

Cornelius C. Shih
Principal Investigator

TABLE OF CONTENTS

SECTION I

EXPERIMENTAL INVESTIGATION OF PRESSURE WAVE PROPAGATION IN A PIPE

SECTION I

EXPERIMENTAL INVESTIGATION OF PRESSURE WAVE PROPAGATION IN A PIPE

ABSTRACT

This study is concerned with the experimental investigation of temporal and spacial velocity profiles in a 3-inch open-end pipe produced by the propagation of nonlinear pressure waves generated by a modified shock tube driver. Using a constant temperature anemometer system with hot-film probes, the investigators measured temporal and spacial velocity profiles at five sections along the 42-ft. test pipe for five diaphragm burst pressures. Data analyzed are presented in graphical form and compared with theoretical results obtained by the method of characteristics through a digital computer. The mathematical model was developed by assuming the flow process isentropic. The discrepancy between the theory and experiment demonstrates the effect of friction upon the dissipation of energy in the flow system.

NOMENCLATURE

a	sonic speed
D	pipe diameter
f	friction coefficient
J	total energy per unit mass
M	Mach number
P	static pressure
q_j	heat flux vector
t	time
V_i and V	velocity vector and component
x	axial coordinate along pipe
γ	ratio of specific heats
ρ	fluid density
θ	temperature
τ_{ij}	stress tensor

INTRODUCTION

Highly intense pressure waves in the near sound field are generated by launch vehicles such as Saturn V. Characteristics of the propagating acoustical energy in the near sound field are highly nonlinear. The use of standard linear scaling techniques for determining environmental criteria such as overall sound pressures and power spectral densities has resulted in considerable error. But there are no adequate scaling procedures available for use in the near sound field.

In order to establish a foundation of scaling laws for the highly nonlinear waves associated with the Saturn V vehicle, the basic knowledge of the relationships among the parameters pertinent to the energy dissipation process associated with the propagation of nonlinear pressure waves in thermoviscous media is definitely required. Review of literature indicates that there are numerous studies in theoretical aspect by Burgers[1], Hopf[2], Cole[3], Lighthill[4], Rodin[5], etc., on the Burgers' equation which is considered to represent the above stated phenomena. There were several studies on wave propagation in pipes by Blackstock[6], Nakamura and Takeuchi[7], Kantola[8], Strunk[9], Sawley and White[10], Brown[11], D'Souza and Oldenburger[12], and Schuder and Binder[13]. These studies are either the treatment of small-amplitude waves, shock waves, plane waves of finite amplitude, or inviscid fluids. Some of them were verified experimentally, but none of them treats the propagation of nonlinear pressure waves of large amplitude with measurements of velocity distributions throughout the pipe.

Specifically, the problem of interest for this study is to experimentally investigate the temporal and spacial velocity profiles of fluid flow in a 3-inch open-end pipe, produced by the propagation of nonlinear pressure waves for various diaphragm burst pressures of a pressure wave generator. As a consequence, temporal and spacial characteristics of wave propagation for a parametric set of nonlinear pressure waves in the pipe containing air under atmospheric conditions were determined.

Velocity measurements at five sections along the pipe of 42 ft. in length were made with hot-film anemometers for five pressure waves produced by diaphragm burst pressures at 20, 40, 60, 80 and 100 psi in the driver chamber of the pressure wave generator. The pressure wave generator, modified from a shock tube, consists of a driver, a piston, and a test pipe. The piston which is advanced at a nearly constant acceleration by the energy released through the mass of air from the shock tube driver generates a pressure wave to propagate through the pipe.

THEORETICAL CONSIDERATION

The physics of the phenomena considered in this study may be expressed by the equations of momentum, energy, continuity, and state as follows:

Momentum: $$\rho \frac{d V_i}{d t} = - \frac{\partial P}{\partial x_i} + \frac{\partial \tau_{ij}}{\partial x_j} \qquad (1)$$

Energy: $$\frac{\partial \rho J}{\partial t} + \frac{\partial \rho V_i J}{\partial x_i} = \frac{\partial P}{\partial t} + \frac{\partial}{\partial x_j}(V_i \tau_{ij} - q_j) \qquad (2)$$

Continuity: $$\frac{\partial \rho}{\partial t} = - \frac{\partial (\rho V_i)}{\partial x_i} \qquad (3)$$

Equation of state for a perfect gas: $$\frac{d P}{P} = \frac{d \rho}{\rho} + \frac{d \theta}{\theta} \qquad (4)$$

Obviously, to date, no exact solutions of the above equations are available because of the extreme complexity. However, they can be simplified somewhat by following limiting assumptions:

1) The flow is one-dimensional; $V = V(x, t)$, $a = a(x, t)$

2) The gas process is isentropic; $\frac{P}{\rho^{\gamma}} = \text{const.}$, $q_j = 0$

3) The fluid is perfect; $\tau_{ij} = 0$

Momentum: $$\frac{\partial V}{\partial t} + V \frac{\partial V}{\partial x} = - \frac{1}{\rho} \frac{\partial P}{\partial x} \qquad (5)$$

Continuity: $$\frac{1}{\rho} \frac{d\rho}{dt} + \frac{\partial V}{\partial x} = 0 \qquad (6)$$

Sonic speed: $$a = \sqrt{\frac{\gamma P}{\rho}} \qquad (7)$$

Proper rearranging of Eqs. (5), (6), and (7) yields the following characteristic equations for the method of characteristics:

$$\left[\frac{\partial}{\partial t} + (V + a)\frac{\partial}{\partial x}\right](V + \frac{2a}{\gamma - 1}) = 0 \qquad (8)$$

$$\frac{dx}{dt} = V + a \qquad (9)$$

left-running characteristics

$$\left[\frac{\partial}{\partial t} + (V - a)\frac{\partial}{\partial x}\right](V - \frac{2a}{\gamma - 1}) = 0 \qquad (10)$$

$$\frac{dx}{dt} = V - a \qquad (11)$$

right-running characteristics

A numerical program was written for temporal and spacial solutions of Eqs. (8), (9), (10), and (11). Results of numerical calculations of the flow field are presented later for qualitative comparison with the experimental results. Listings of the numerical program for cases without and with friction are presented in the Appendix A. The numerical program for the case with friction was formulated based on Eq. (12).

DESCRIPTION OF TEST FACILITY

1. Pressure Wave Generator

The pressure wave generator generates pressure waves in a long test pipe by accelerating an aluminum piston over an 11-inch distance from the inlet end of the test pipe. The aluminum piston is accelerated by a driver system which is located at a respectable distance from the test pipe. Also, the aluminum piston has no direct contact with the inside surface of the test pipe at any time. This arrangement insures that no shocks or vibrations are transferred to the test pipe.

The pressure wave generator consists of three major parts:

1. Driver Section, 6.6 ft long
2. Piston Section, 3.2 ft long
3. Test Pipe, 42.2 ft long .

The overall length of the test facility amounts to 52.0 ft. All sections are mounted on support stands; the height of the centerline of the tubes and the movable parts is 49 in. The inside diameter of the driver section and the test pipe is 3 in.

a. Driver Section

The driver tube of the shock tube facility at The University of Alabama in Huntsville is used as driver section of the pressure wave generator. Figure 1 shows the driver section with its measuring and control devices. The basic unit is a constant-area stainless steel tube of 3 in. inside diameter. The tube including the diaphragm section and the pressure supply system is mounted to a support dolly that is movable on a track. The driver tube may be operated at controlled pressures up to 2,000 psi by using a double-diaphragm technique.

In this project, however, a diaphragm bursting technique was developed for relatively low burst pressures. The diaphragm was made of mylar sheets. The steel wire attached to the diaphragm was electrically heated and bursted the diaphragm immediately. This method has proved to be reliable for the burst pressures ranging from 20 to 100 psi.

b. Piston Section

This section converts the driver pressure in piston motion which generates the pressure wave within the test pipe. The piston section is shown in Figures 2 and 3; also, the technical details are given in the assembly drawing of Figure 5. As it can be seen from the photograph of Figure 2, a stainless steel tube with a welded flange is connected to the diaphragm section of the driver tube. A steel piston of 3 in. diameter is driven within the steel tube (see Figure 5). This piston is attached to one end of a bearing shaft by means of a screw thread, while the other end of the bearing shaft is screwed into an aluminum piston that moves within the test pipe during the operation. The bearing shaft consists of a cold finished carbon steel with relatively high tensile strength (161,500 psi).

The piston system is accelerated over a distance of 11 in. while it is subject to the driver pressure. Then, the piston system is slowed down by a double-acting damping system within a distance of 6 in. The piston finally comes to rest by a heavy stopper block. The damping system is built as an integral part of the stopper block using the combined effects of 40 springwashers and a shock absorbing air cushion generated by a steel piston sliding in a cylinder of the stopper block.

Two plain bearings are installed between the stopper block and the test pipe. They serve as a guidance for the bearing shaft which moves into the test pipe. In addition to the two bearings, the piston system is in fact supported at three more locations due to the design and the precision machining of the matching parts. These five supports make the bearing shaft of the piston system a statically indeterminate structure.

The decleration and stopping of the piston system resulted in a variety of unexpected major problems due to the heavy impact. These difficulties could be solved through modifications of the facility.

c. Test Pipe

A galvanized steel pipe of nominal pipe size, 3.000 in., schedule number 40, is used as test pipe. The steamless pipe consists of two basic parts which are connected by means of a screw joint. Figure 4 shows the test pipe in a general view; also, the beginning of this pipe is shown in Figure 2.

The inside diameter of the test pipe is 3.068 in. The aluminum piston generating the pressure wave has a diameter of 3.000 in.; thus there is a gap between the piston and the pipe of 0.034 in. This gap of approximately 1/32 in. amounts only to be approximately 1/90 of the pipe diameter. Because there is no metal contact between the moving piston and the test pipe, no shocks or vibrations from the driver system can be transferred to the metallic test pipe. This insures that the instrumentation is free of any other influence but the air flow within the pipe.

In order to measure velocity profiles generated by the pressure wave, five instrumentation ports have been machined at five sections along the 42 ft. test pipe. A brass fitting is screwed into each port with the hot film probe. The first port is located in a distance of 3 ft. from the beginning of the test pipe. Each of the following instrumentation ports has an equal distance of 8 ft. from each other. Behind the last instrumentation port, the remaining pipe section turns out to be 7 ft. 3 in. in length.

Additional instrumentation ports were machined in three pipe sections at the end of the investigation period. This permits the installation of two hot film sensors in the same pipe section opposite to each other.

2. Instrumentation System

Five Hot Film Sensors in connection with Constant Temperature Anemometers were used to measure velocity profiles of the unsteady flow of air in the test pipe. The five sensors were mounted into instrumentation ports by brass fittings. The instrumentation ports are spaced at intervals of 8 ft. on the upper side of the test pipe. The details of sensor installation and the positioning of the sensing element are shown in Figure 6. The sensor-anemometer system was connected with a recording oscillograph. This recorder transfers the electrical output data to immediately readable photographic records.

a. Sensor System

The sensing element of a hot film sensor is essentially a conducting film on a ceramic substrate, e.g., a quartz coated platinum film on the surface of a glass rod. Gold plating on the ends of the rod isolates the sensitive area and provides a heavy metal contact for fastening the sensor to the needle supports. The thickness of the metal film on a typical film sensor is less than 1000 Angstrom units. The physical strength is provided by the substrate material, and a thin quartz coating on the surface resists acculdlation of foreign material. Hot wire sensors are probes of similar nature; however, the hot film sensors have several advantages like better frequency response and more flexibility with respect to sensor configuration, when they are compared with hot wire sensors.

The sensors are designed for use with a constant temperature anemometer circuit. A constant temperature anemometer measures the instantaneous heat transfer rate (heat flux) between a small electrically heated sensor and the flow being measured. An electronic feedback control circuit varies the electrical current through the sensor to correspond to the cooling effect of the flowing fluid, always keeping the sensor at a constant resistance and temperature.

In this project, we used a constant temperature anemometer system including sensors, of Thermo-Systems Inc., along with the Monitor Power Supply Unit (Model 1031-10A) for ten channel operation.

Each of the five hot film sensors was a part of a controlled bridge or anemometer circuit. For this purpose, we employed five units of Model 1033A Anemometer Module. Some specifications of the Model 1033A Anemometer are as follows: bridge voltage output 0 to 24 VDC: output impedance 50 ohms; frequency response 0 to 3 kcps.

An important element in the bridge circuit is the control resistor which is used to set the sensor operating temperature and to provide temperature compensation. The control or compensating resistor is an external fixed resistor taking into account an overheat ratio of 1.5 (operating resistance to room temperature resistance on the sensor) and, in addition, a bridge ratio of 1/5 (hot sensor to compensating resistance). In order to determine the room temperature resistance of each sensor system including its long connecting cable, a Variable Decade, Model 1056 was used. The resulting compensating resistor was plugged into the anemometer module. The output signal of the bridge is a voltage in relationship to velocity or mass flow units. This relationship has to be determined by individual calibration of each sensor system.

The sensor selected has the following specifications: The Quartz Coated Hot Film Sensor is cylindrical and has needle supports (Model 1212-20); the diameter is 0.002 in.; the length is 0.040 in.; the relative frequency response is 40,000 cps; the nominal resistance is 4-8 ohms. The needle supports of the sensor have a 90° bend to probe shank, facing upstream for reduced flow disturbance.

b. Recording Equipment

Five channels of voltage outputs from the anemometer system were recorded on an oscillograph (Type - CEC Datagraph 5-133). This recorder was operated in conjunction with a Galvanometer Amplifier, Model T6 GA -500 from Honeywell; also, five D.C. Amplifiers 1-165 from CEC were used. The Recording Oscillograph (Type 5-133) may accommodate frequency variations up to 13,000 cps. The recorder was operated at the maximum writing speed of 160 inch/sec. Only this fast writing speed made it possible to obtain recording data that could be clearly analyzed. The electronic flash timing system produced 100 lines per second. The error in timing was determined to be less than 0.5 percent.

The galvanometers used in the oscillograph were CEC Fluid Damped Galvanometers (Type 7-326). They have an undamped natural frequency of 5,000 cps and a system voltage sensitivity of 0.291 in/volts.

The frequency response of the entire instrumentation system is limited by the anemometer circuit. As mentioned before, the anemometers used have a frequency response up to 3,000 cps. This is at least 100 times greater than it is required for the case of 100 psi burst pressure.

TEST PROCEDURE

1. Calibration of the Instrumentation System

A careful calibration of the complete instrumentation system was performed before each test series. The basic variable measured by a hot film sensor is the voltage related to the rate of heat transfer from the sensing element to the flow of air in the test pipe. Because all hot film sensors are not exactly the same in response characteristics, a calibration curve of each individual sensor system was obtained for establishing the relationship between the flow velocity and the deflection recorded due to voltage output. This relationship was highly nonlinear, therefore, about 10 to 15 calibration points were recorded for each curve.

The Model 1125 Calibrator of Thermo-Systems Inc. was used along with a precision manometer and a thermometer. The sensor and recording system includes all cables and connections as it is used during the test. The probes are fastened on the calibrating device in front of a small nozzle which is fed by two quieting chambers in series. The calibrator is part of a flow system in which the delivery pressure is regulated and the pressure difference across the calibrator nozzle is measured. During the calibration procedure, the flow in the system was controlled in such a way that certain pressure differences across the nozzle were generating known velocities in this nozzle. The pressure difference was measured by a precision manometer while, at the same time, the oscillograph recorded the deflection produced by the voltage output of the combined sensor-anemometer and recording system. It should be noted that all deflections were measured in units of length (not in units of voltage). The flow velocity was calculated by a computer program. Input data were the pressure difference, the temperature in the stilling chamber and the ambient pressure.

2. Conducting the Test

The driver and piston sections were subject to careful inspection before every test. In particular, the piston system was checked for its smooth movement within the test pipe and its initial position. After the positioning of the sensors was also inspected, the driver section with a mylar diaphragm was then pressurized to a desired pressure (20, 40, 60, 80, or 100 psi). As the exact pressure measured by a precision pressure gage was reached in the driver section, the sensor-anemometer system was turned to "run"- position, and the operation of the oscillograph was started. The record drive system of the recorder needed approximately two seconds for acceleration, until the diaphragm was bursted by electrically heating a circled wire attached to the diaphragm. Recording of the voltage outputs from the anemometers was then accomplished.

Pertinent data collected from the tests are tabulated and presented in Appendix B.

PRESENTATION AND DISCUSSION OF EXPERIMENTAL DATA

1. Test Conditions

The test medium in the test pipe was air at atmospheric conditions. Average temperature and pressure of the test medium were 75° F and 29.56 in Hg absolute under the static condition throughout the test.

The piston system was accelerated over a distance of 11 inches in all cases. In each test, the piston system came completely to rest after it underwent a retardation process for a 6-inch distance. The driver medium of the piston system was compressed air.

The total number of tests conducted was over one hundred. The tests were performed at five burst pressures, 20, 40, 60, 80, and 100 psig, employing five different sensor positions across each of the five pipe sections. Figure 6 shows Sensor Positions A, B, C, D, and E across a pipe section. The experimental data are presented in graphical form with a limited analysis of the data. The results presented were taken from approximately 35 selected tests.

2. Oscillograph Recording

Figure 7 shows a typical oscillograph recording from the five sensors located at five sections along the test pipe. Each single record presents flow velocity in terms of voltage output versus time. The time base is 10 milliseconds per division, moving horizontally from right to left.

Figure 7 clearly demonstrates two basic phenomena which are associated with each other:

1. A pressure wave is generated by the piston system. This pressure wave travels through the test medium with approximately the speed of sound.
2. The pressure wave causes a motion of the air particles which are originally at rest.

The starting point of the deflection for each section indicates that the pressure wave has reached the corresponding sensor in the test pipe. Consequently, the time difference between the starting point of two neighboring sections can be used to calculate the mean velocity of the wave propagation between these sections.

For instance, the time difference between the initial recording points of Sections 1 and 2 (Figure 7) is $t_{1,2} = 6.8$ milliseconds. Since all sensors are spaced at intervals of 8 ft., the mean velocity of the pressure wave between Section 1 and Section 2 is 1176 ft/sec.

The recorded deflection of every section shows qualitatively that the flow generated by the pressure wave undergoes an acceleration during the time t_a (see Section 3 in Figure 7). The maximum deflection is reached at the end of the acceleration phase. Thereafter, irregular deflections are recorded, but they are not of interest for this study. In the case of Section 3 (Figure 7), the acceleration phase took 17.2 milliseconds. Since the calibration curves are different for each sensor system, the absolute value of the deflection for the different sections cannot be compared with each other on the oscillograph recording.

3. Data Analysis

Results are presented and discussed in the following aspects:

a. Temporal velocity profiles
b. Spacial velocity profiles
c. Acceleration of the fluid flow
d. Propagation speed of the pressure wave
e. Comparison of numerical calculations with experimental data
f. Blockage effect

a. Temporal Velocity Profiles

Temporal velocity profiles in five pipe sections are presented in Figures 8 through 14. In these figures the flow velocity in ft/sec is plotted against the test time in milliseconds. The evaluation has been done step by step at intervals of one millisecond. Each curve starts with the initial point of the deflection and is terminated by the end of the acceleration phase. Therefore, the end of each plotted curve is the maximum recorded deflection which represents the maximum measured flow velocity (see Section 3 in Figure 7). The time scales of Figures 8 through 14 are set relative to the time of wave arrival at Section 1.

Figure 8 shows temporal velocity profiles at Sensor Position A for burst pressures at 100 and 40 psi. Sufficient number of repetitions, say more than three, was made on each test to ensure the repeatability and consistency of the data. Comparison of the two sets of profiles indicates that decay of the pressure wave is more notable for the case of 40 psi after Section 3. The case of 100 psi seems to indicate that the wave propagation in this length of pipe yields less decay. The curves presented in Figure 8 are almost linear after a very short period of increasing acceleration. This is true for both cases, 100 and 40 psi, and for Sections 1 through 4. Following the short period of increasing acceleration, the measured fluid flow was noted in all cases to be fairly constant in acceleration before the piston is stopped. The maximum velocity measured in the different pipe sections seems to depend very little upon the pipe length. A slight irregularity of the profile at Section 3 has been determined to be strictly instrumental by comparative tests with other sensors installed at the same section.

The velocity profile at Section 5 was found to be nonlinear. The increasing acceleration of the propagated wave recorded at Section 5 for both pressures was caused by the expansion wave reflected negatively from the pipe exit. With the propagation speed of approximately 1100 ft/sec, the pressure wave took about 10 milliseconds to reflect back from the pipe exit to Section 5, causing the flow to accelerate at a greater rate.

The steep bends occurred on the velocity profile at Section 5 is considered to be primarily caused by the wave reflection at the pipe exit. In order to ascertain this, several identical tests were performed for a 21-ft. pipe of the same diameter. Test results of velocity profiles from the 21-ft. pipe are presented in Figure 9 for comparison with data from the 42 ft. pipe under the same test conditions. The velocity profile at Section 3, which is closest to the exit of the 21-ft. pipe, is shown to be characteristically similar to the velocity profile of Section 5 near the exit of the 42-ft. pipe. It must be considered, however, that the distance between Section 3 and the pipe exit of the 21-ft. pipe is only 2 ft. in length; in comparison with it, the distance between Section 5 and the pipe exit of the 42-ft. pipe is 7 ft. 3 in. in length. For this reason, the effect of wave reflection is recorded to be more intense at Section 3 (and also affecting Section 2) of the 21-ft. pipe as it is the case at Section 5 of the 42-ft. pipe. This comparison of data from two different pipe lengths evidently illustrates the cause of peculiarity of the velocity profile at the section near the pipe exit.

Figures 10, 11, 12, 13, and 14 depict temporal velocity profiles for Sensor Positions A, D, and E at each of five sections respectively, for burst pressures of 100, 80, 60, 40, and 20 psi. These figures show that velocity distributions are not uniform across the pipe section in all cases. It is significant to note that the velocity near the pipe wall has been measured to be slightly higher than the one near the center. The existence of these phenomena was ascertained by repeated measurements under the same test conditions.

Figures 8 through 14 also reveal a clear trend with respect to the duration of the acceleration period which is markedly different for cases with different burst pressures. Because the piston was accelerated over the same distance of 11 inches in all cases, the time needed for the acceleration process is longer for the case of a smaller acceleration due to a lower burst pressure. The duration of the acceleration process depends little upon the sensor location in the test pipe, even though a slightly decreasing trend can be observed in the direction of the propagating pressure wave.

b. Spacial Velocity Profiles

Spacial velocity profiles are presented in Figure 16 which also demonstrates in a different form these peculiar phenomena of velocity distributions across Section 1 and 2 for two time frames respectively, at 100 and 20 psi burst pressures. Having determined through sensor calibrations that all hot-film sensors were functioning with a reasonable accuracy, say less than 15% in error, the investigators have determined that the peculiar phenomena may be due to the energy dissipation caused by frictional resistance along the wall, or perhaps due partly to the space gap existing between the piston and the test pipe. The effect of friction has been considered predominant to the phenomena. However, further investigations and data analysis based on the consideration of energy balance and pressure distribution are required before making conclusive statements on these phenomena.

c. Acceleration of the Fluid Flow

The accelerations of the fluid flow caused by the wave propagation in the pipe were calculated for various burst pressures at Section 1 with Sensor Position A as a typical example. The resulting accelerations are plotted against time in milliseconds in Figure 15. In a very short time, say less than 5 milliseconds, the acceleration seems to rise from rest to a high value which increases as the burst pressure increases. After the short rise time, the acceleration appears to remain constant in the duration of piston acceleration for all pressures. High rates have been found for the acceleration of the gas particles due to the pressure wave. For the case of 100 psi burst pressure, e.g., the acceleration is approximately 4500 ft/sec^2; this is 140 times the gravitational acceleration.

d. Propagation Speed of the Pressure Wave

Figure 17 presents propagation speeds of the pressure waves varying along the pipe for five burst pressures. The time difference between the starting points of two neighboring sections was used to determine the mean speed of the propagating pressure wave between these sections. The propagation speed was noted to remain constant for most cases with the statistical mean of 1100 ft/sec and the variance of less than 25 ft/sec^2. For comparison with it, the speed of sound ranges from 1130 to 1136 ft/sec for slightly varying laboratory temperatures between 72 and 78° F.

No correlation among the axial pipe distance, the burst pressure and the propagation speed was obviously noted. It must be mentioned, however, that it is necessary to employ different instrumentation and recording methods in order to get more accurate results with respect to the propagation speed.

e. Comparison of Numerical Calculations with Experimental Data

Temporal velocity profiles were numerically calculated using the method of characteristics, (Eqs. 8-11), with measured boundary conditions from the piston movement. These results are compared with the experimental data for burst pressures of 80, 60, 40, and 20 psi in Figures 18 through 21. The calculations were carried out with the use of UNIVAC 1108 electronic computer. The piston movement was recorded and analyzed with a Fasta high speed movie camera at the rate of approximately 4500 frames per second.

Because the mathematical model was established based on isentropic assumptions, the experiment clearly demonstrated that the flow process associated with the wave propagation was not isentropic, observing a significant effect of frictional resistance against the flow which is subsonic throughout the pipe. As the energy dissipation takes place along the pipe, the static pressure tends to decrease along the pipe while the velocity decreases rather significantly at a fixed position comparing with the isentropic case. These phenomena can be illustrated qualitatively by the following equation modified from Equation (1) for unsteady one-dimensional flow in a pipe with friction:

$$\frac{\partial V}{\partial t} = -\frac{1}{\rho}\frac{\partial P}{\partial x} + \frac{1}{\rho}\frac{\partial \tau_w}{\partial x} - V\frac{\partial V}{\partial x} \qquad (12)$$

where $\tau_w = \tau_{ij} \approx f\ \rho\frac{V^2}{2}$: shearing stress along the pipe wall. While the convective acceleration, $V\frac{\partial V}{\partial x}$ is experimentally known to be reasonably small in this case, and a minor positive contribution to $\frac{\partial V}{\partial t}$ is made by the increase in negative pressure gradient, a predominant negative contribution to the temporal acceleration, $\frac{\partial V}{\partial t}$ is made by the shearing stress term as demonstrated in Figures 18 through 21.

It is noteworthy that a greater deviation of the experimental velocity profile from the calculated isentropic data was observed for the cases at lower burst pressures, agreeing with the theoretical consideration based on Equation (12). Also, it is significant to note that the wave fronts of all cases propagated nearly isentropically as evidenced by the close agreement shown in Figures 18 through 21.

On the other hand, both Figures disclose a difference in the rate of acceleration between the calculated and the experimental velocity profiles. The calculated profiles show the greatest acceleration at the beginning of the flow process. The calculations are based on the experimentally determined piston motion.

Figures 22 and 23 present a comparison of numerical calculations with and without friction at burst pressures of 40 and 80 psi. The calculations considering friction were made with a friction coefficient of $f = 0.2$. The rate of acceleration is found to be subject to the influence of friction. This influence is small in the pipe section near the piston; but the effect of friction is growingly pronounced in the direction of propagation of the pressure wave.

f. Blockage Effect

Additional tests were performed in order to investigate whether or not blockage effect of the probes may cause or contribute to the peculiar velocity distribution across each pipe section. The probe support has a frontal area of 2.5% referred to the pipe cross-section if the sensing element is in Position A. In contrast to this, the frontal area of the probe support is negligible when the sensing element is in Position E.

In order to keep the blockage effect approximately constant for different sensor positions, a dummy probe was installed in Section 3 opposite to the measuring probe. The sensing element of the dummy probe had a distance of 1/4 inch from the sensing element of the measuring probe in all positions. No other probes were in front of Section 3 at the time of these measurements.

Figures 24 and 25 present results of the measurements with dummy probe compared with data from earlier tests without dummy probe at burst pressures of 80 and 40 psi. Both figures clearly reveal that blockage has a predominant influence on the velocity profile, because the velocities measured without dummy probe are greater at any time frame than the corresponding data with dummy probe. This is also confirmed by the observation that the velocity difference due to blockage is recorded to be definitely higher for Sensor Position E as it is the case for Sensor Position A in both cases 80 and 40 psi.

On the other hand, the results shown in Figures 24 and 25 additionally verify our earlier findings as presented in Figures 10 to 14, that the velocities recorded at Sensor Position E are greater than the data measured at Sensor Position A. It appears that some other effects are still causing the difference between the measurement results at Sensor Positions A and E, but these other effects are found to be not as predominant as the blockage effect.

REFERENCES

1. Burgers, J., "A Mathematical Model Illustrating the Theory of Turbulence," Advances in Applied Mechanics, Academic Press, 1948.

2. Hopf, E., "The Partial Differential Equation $u_t + u u_x = \mu_{xx}$," Communications on Pure and Applied Mathematics, Vol. III, pp. 201-230, 1950.

3. Cole, J. D., "On a Quasi-Linear Parabolic Equation Occurring in Aerodynamics," Quarterly of Applied Mathematics, Vol. IX, No. 3, pp. 225-236, Oct. 1951.

4. Lighthill, M. J., "Surveys in Mechanics," edited by G. K. Batchelor and R. M. Davis, Cambridge University Press, pp. 250-351, 1956.

5. Rodin, E. Y., "Propagation of Waves of Finite Amplitude in Thermoviscous Media," Report WR66-37, Wyle Laboratories under Contract NAS8-11312, "Propagation of One and Two-Dimensional Waves of Finite Amplitude," Report WR67-18, Wyle Laboratories under Contract NAS8-21060.

6. Blackstock, D. T., "Propagation of Plane Sound Wave of Finite Amplitude in Nondissipative Fluids," J. of Acoustical Society of America, Vol. 34, No. 1, pp. 9-30, Jan. 1962.

7. Nakamura, A. and Takeuchi, R., "Propagation of Sound Pulses Through Pipes," Acustica, Vol. 22, pp. 88-95, 1969-70.

8. Kantola, R., "Transient Response of Fluid Lines Including Frequency Modulated Inputs," ASME Paper No. 70-WA/Flcs-1.

9. Strunk, R. D., "Transient Response of Fluid Lines Through Use of Infinite Products," ASME Paper No. 70-WA/FE-22.

10. Sawley, R. J. and White, P. H., "Energy Transmission in Piping Systems and Its Relation to Noise Control," ASME Paper No. 70-WA/Pet-3.

11. Brown, F. T., "The Transient Response of Fluid Lines," J. of Basic Engineering, Trans. ASME, Series D, Vol. 84, No. 3, p. 547, Dec. 1962.

12. D'Souza, A. F. and Oldenburger, R., "Dynamic Response of Fluid Lines," J. of Basic Engineering, Trans. ASME, Series D, Vol. 86, No. 2, pp. 589-598, Sept. 1964.

13. Schuder, C. B. and Binder, R. C., "The Response of Pneumatic Transmission Lines to Step Inputs," J. of Basic Engineering, Trans. ASME, Series D, Vol. 81, No. 4, p. 578, Dec. 1959.

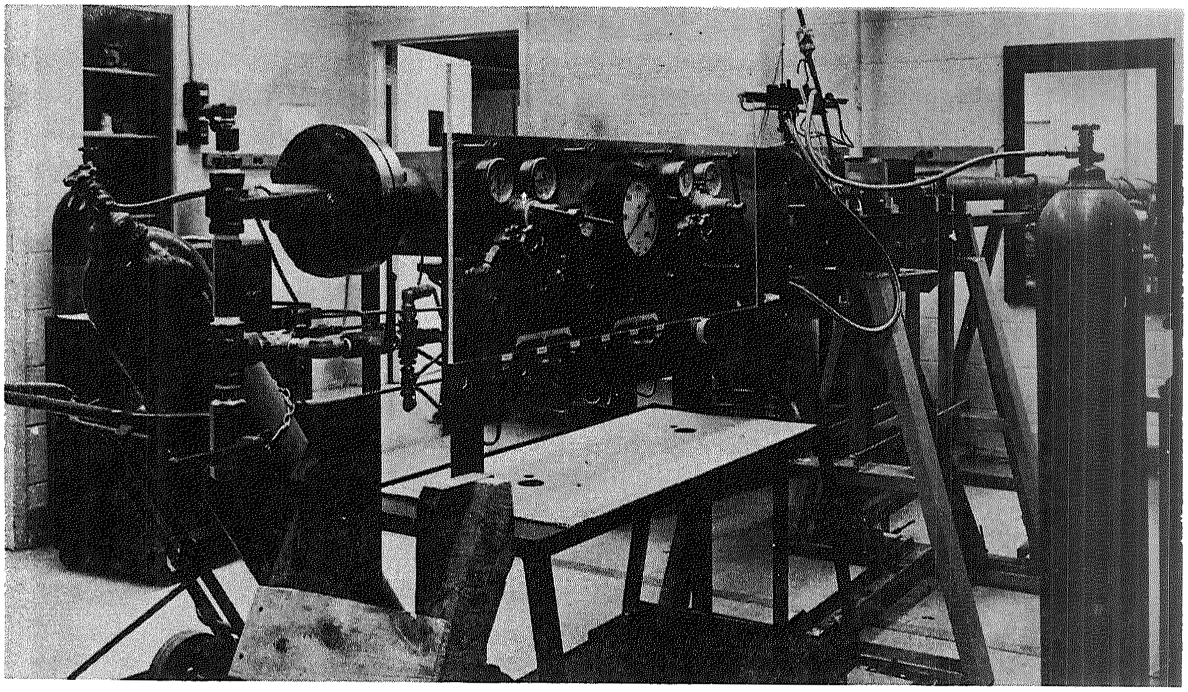

Fig. 1 General View of Driver Section of Pressure Wave Generator.

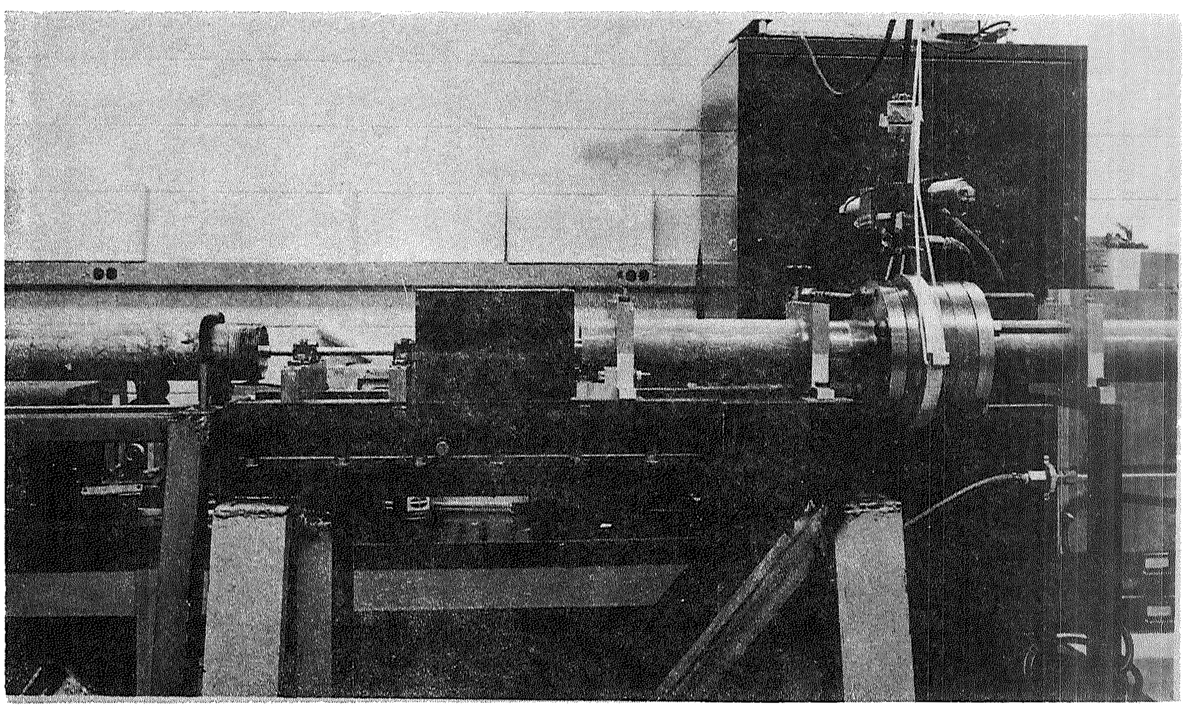

Fig. 2 General View of Piston Section with Stopper Block (center), Driver Section (right), and Test Pipe (left).

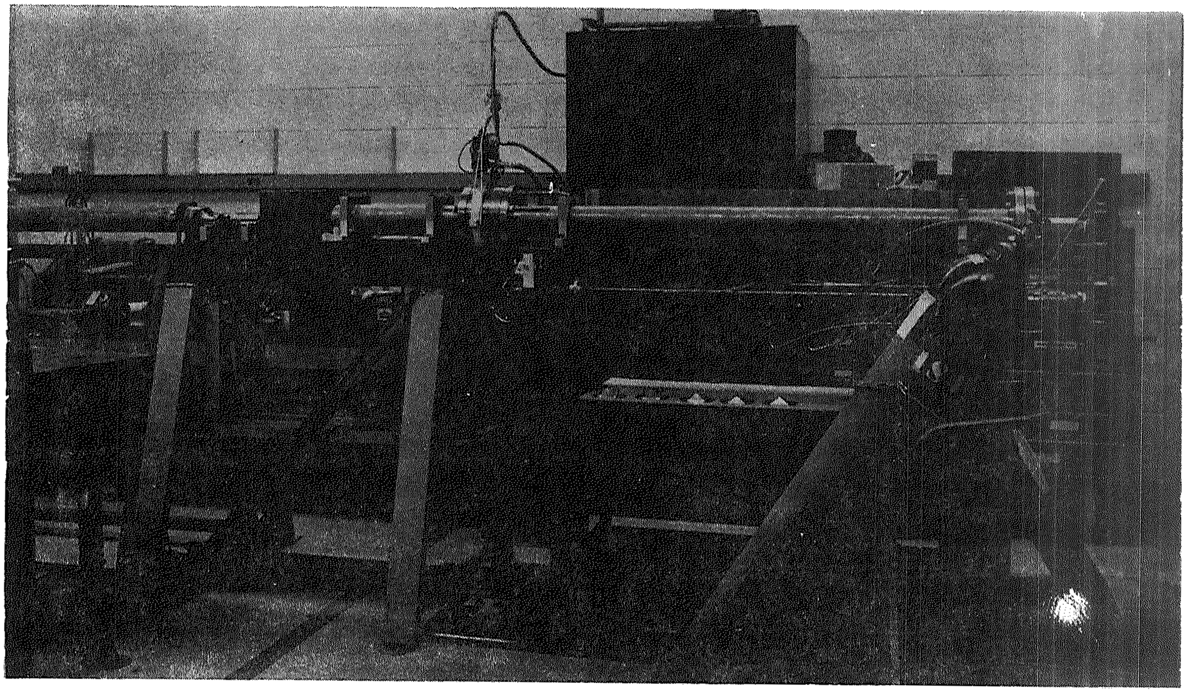

Fig. 3 General View of Driver Section (right), Piston Section and Test Pipe (left) of Pressure Wave Generator.

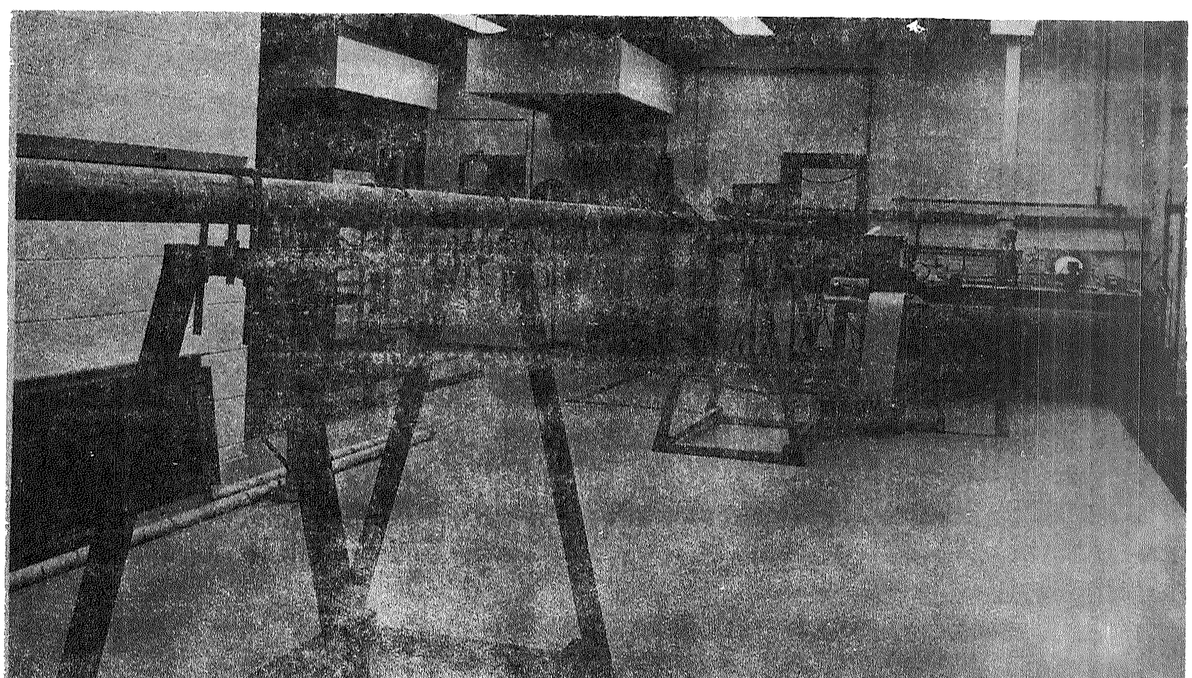

Fig. 4 General View of Test Pipe.

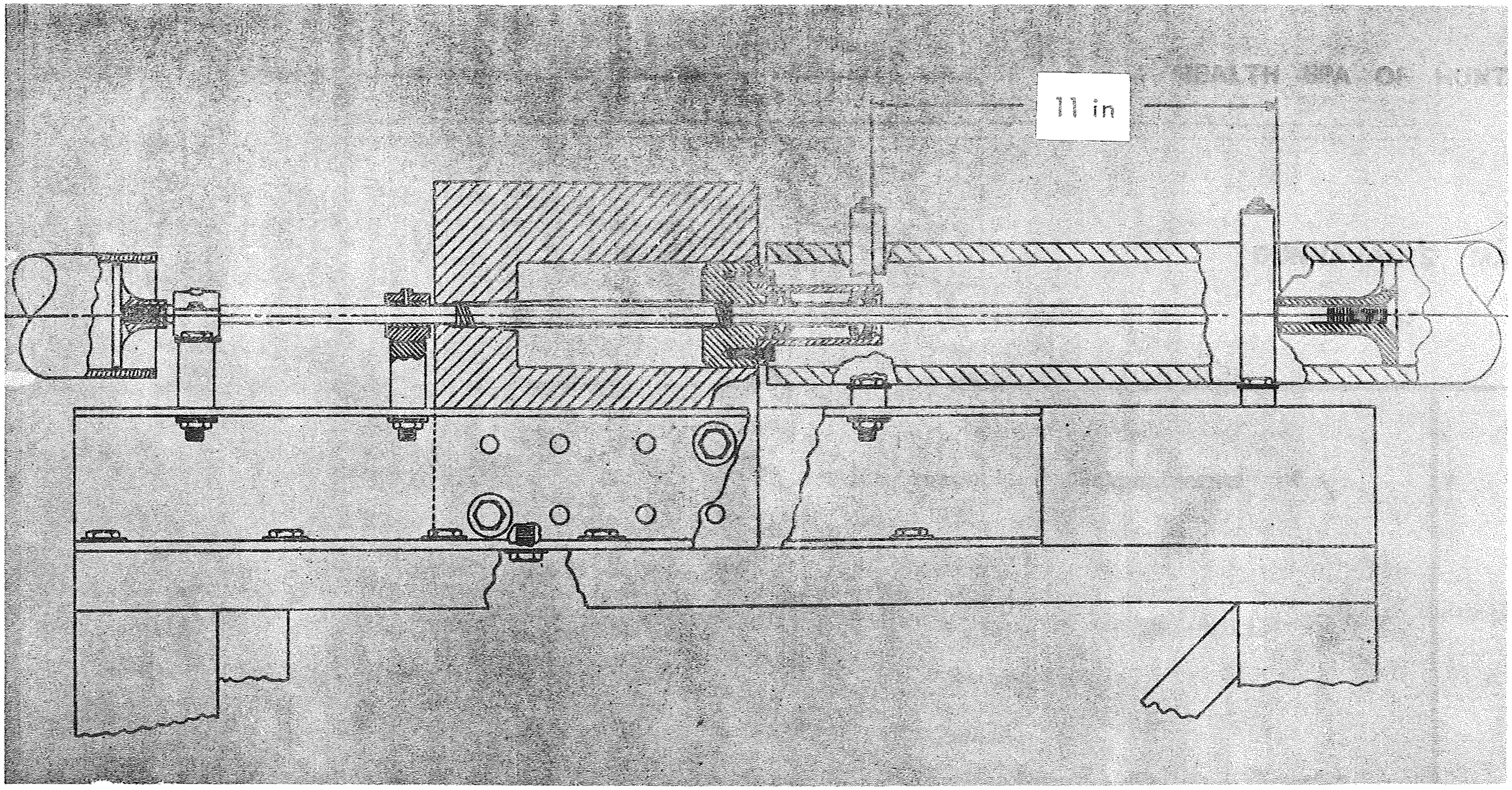

Fig. 5 Crossectional Diagram of Piston Section with Stopper Block (center), Driver Tube (right), and Test Pipe (left). The Acceleration Distance of the Piston System (11 in) is Noted Above.

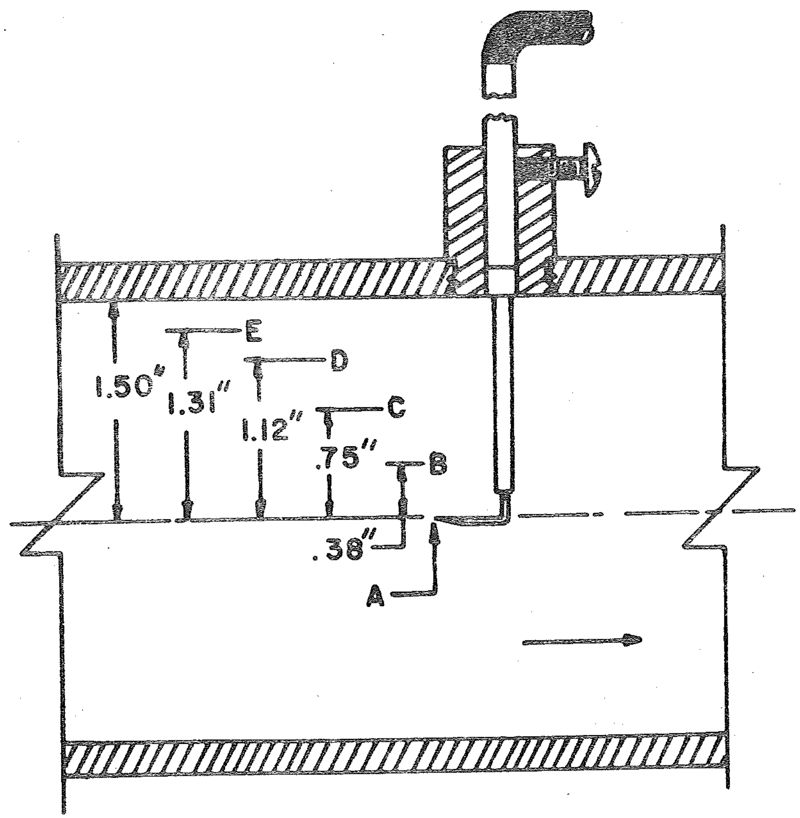

Fig. 6 Diagram of Hot Film Sensor Installation and Positioning of Sensor Element.

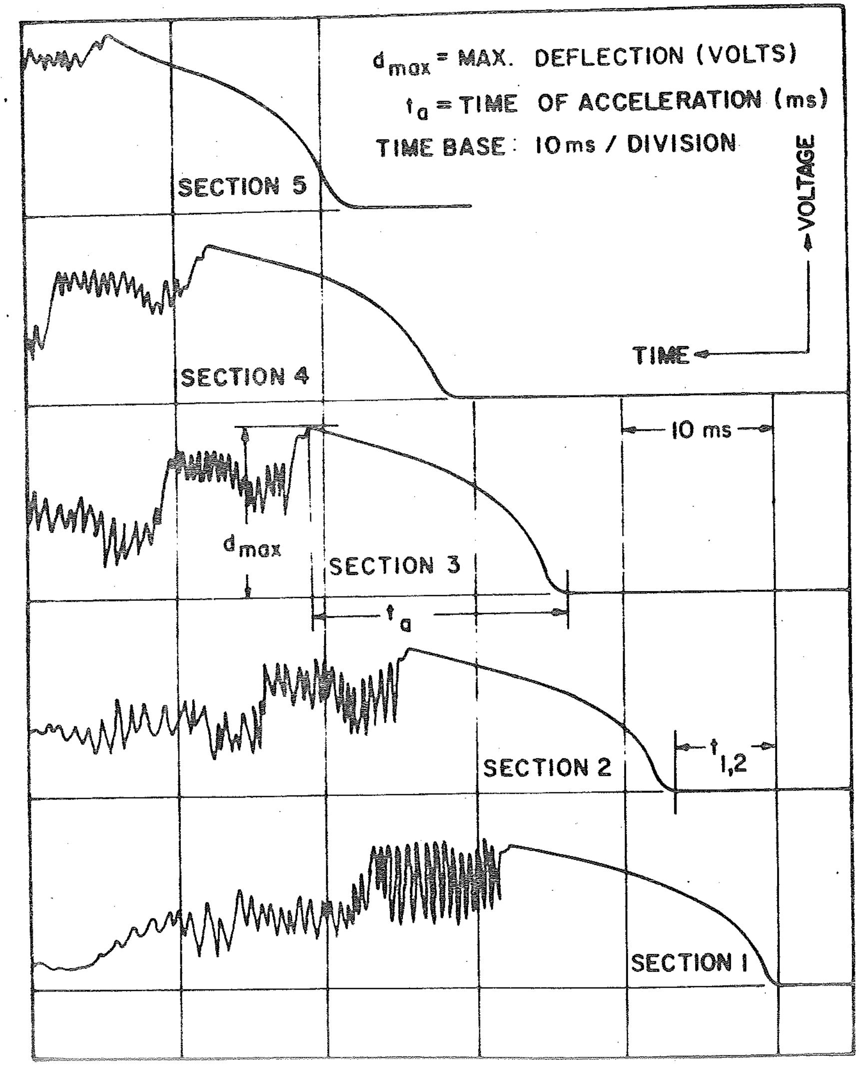

Fig. 7 Typical Oscillograph Recording.

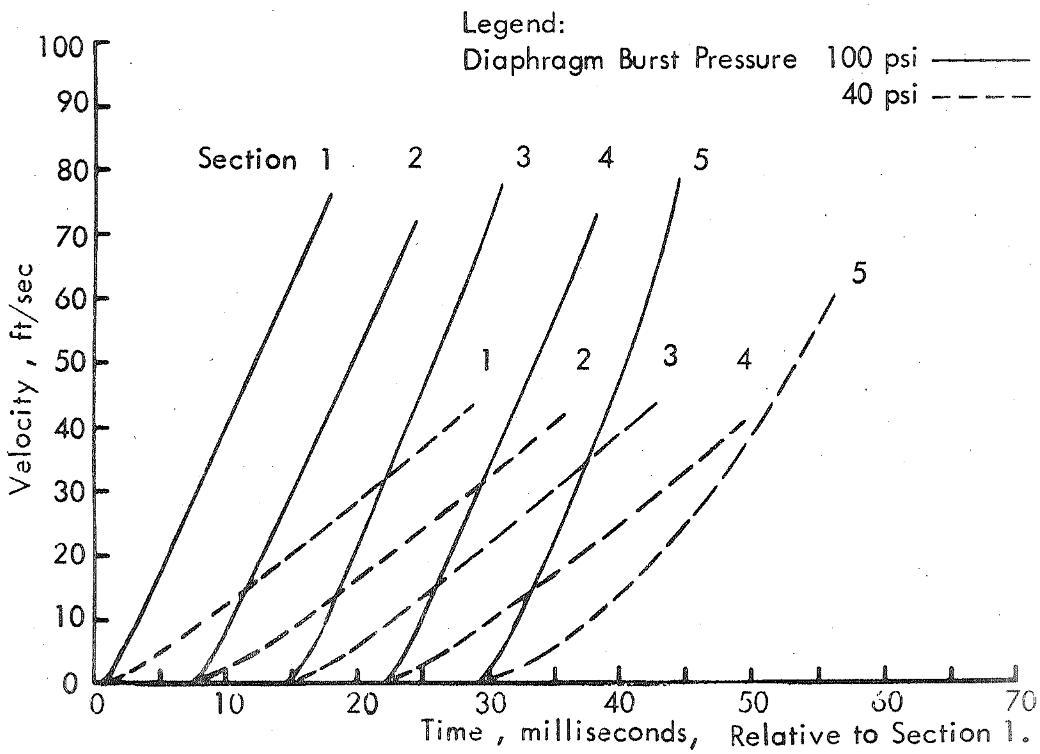

Fig. 8 Flow Velocity Versus Time at Sensor Position A in 5 Pipe Sections for Diaphragm Burst Pressures at 100 and 40 psi.

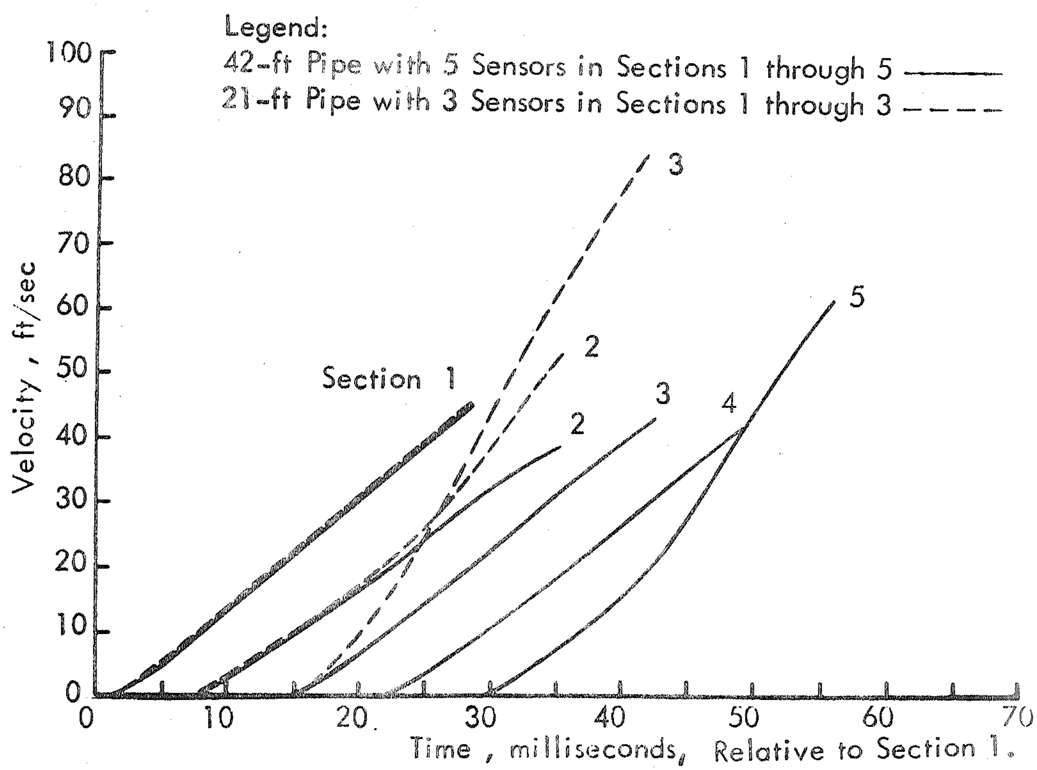

Fig. 9 Flow Velocity Versus Time for 2 Different Pipe Lengths at Diaphragm Burst Pressure of 40 psi.

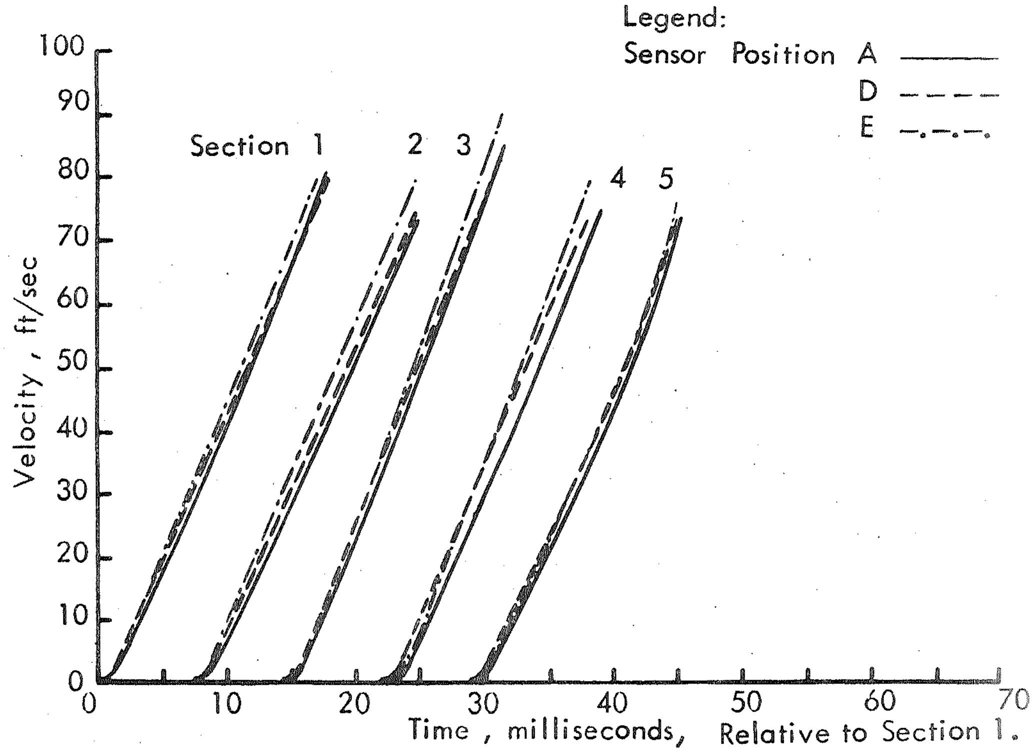

Fig. 10 Flow Velocity Versus Time for Various Sensor Positions at Diaphragm Burst Pressure of 100 psi.

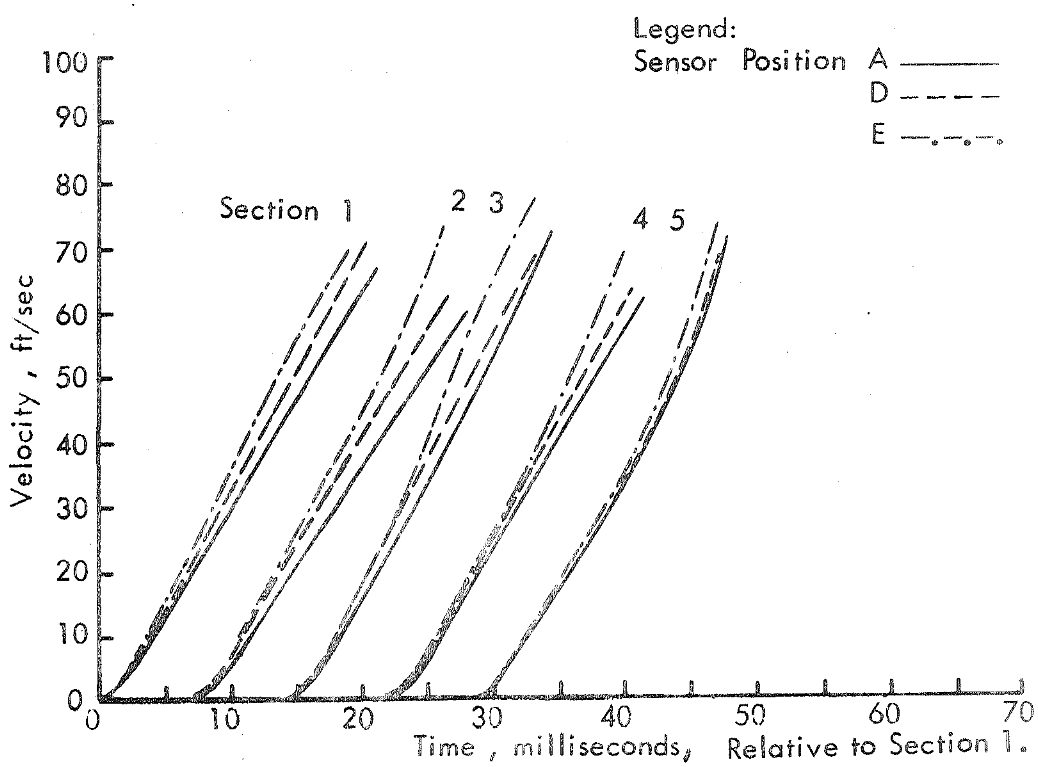

Fig. 11 Flow Velocity Versus Time for Various Sensor Positions at Diaphragm Burst Pressure of 80 psi.

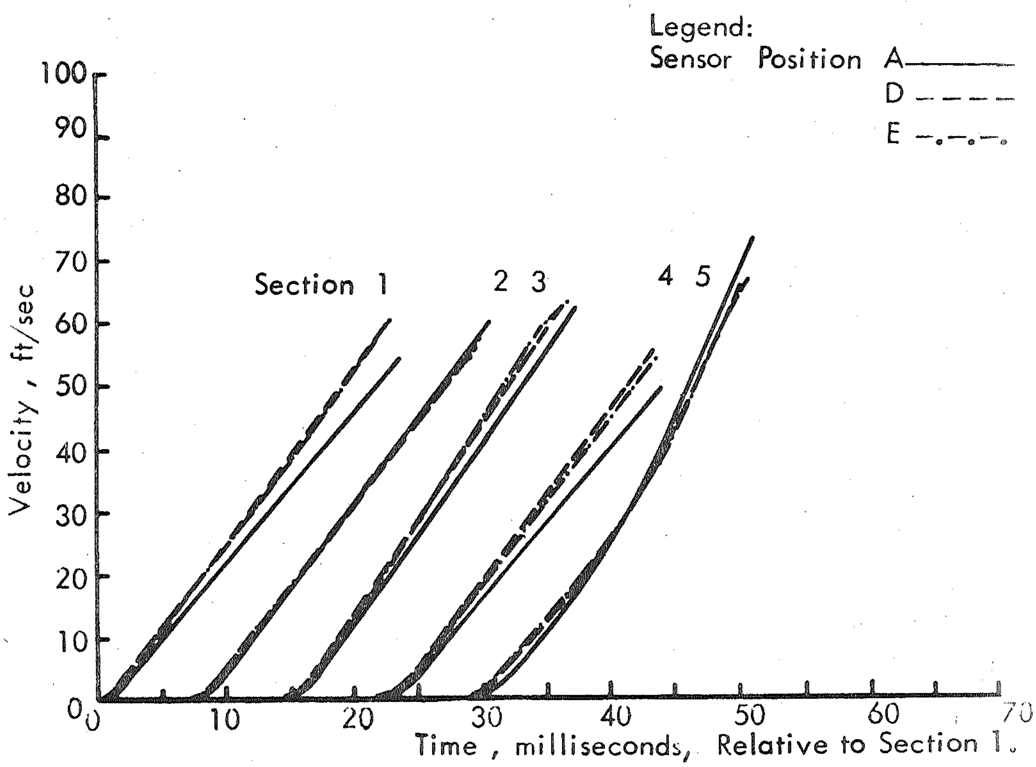

Fig. 12 Flow Velocity Versus Time for Various Sensor Positions at Diaphragm Burst Pressure of 60 psi.

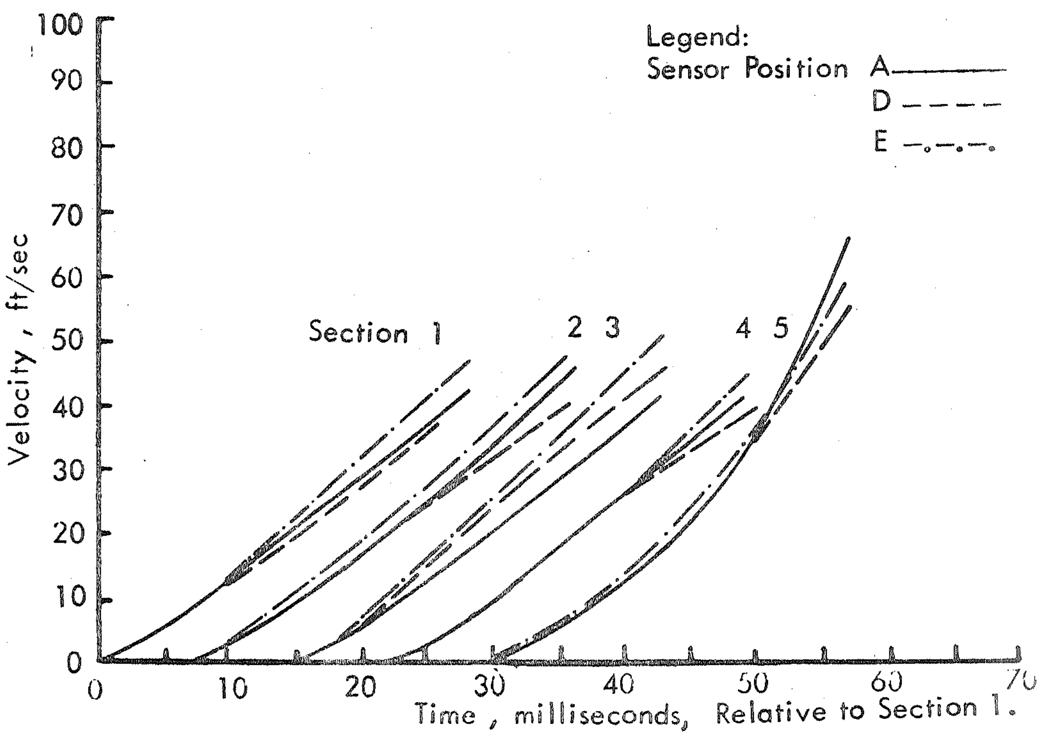

Fig. 13 Flow Velocity Versus Time for Various Sensor Positions at Diaphragm Burst Pressure of 40 psi.

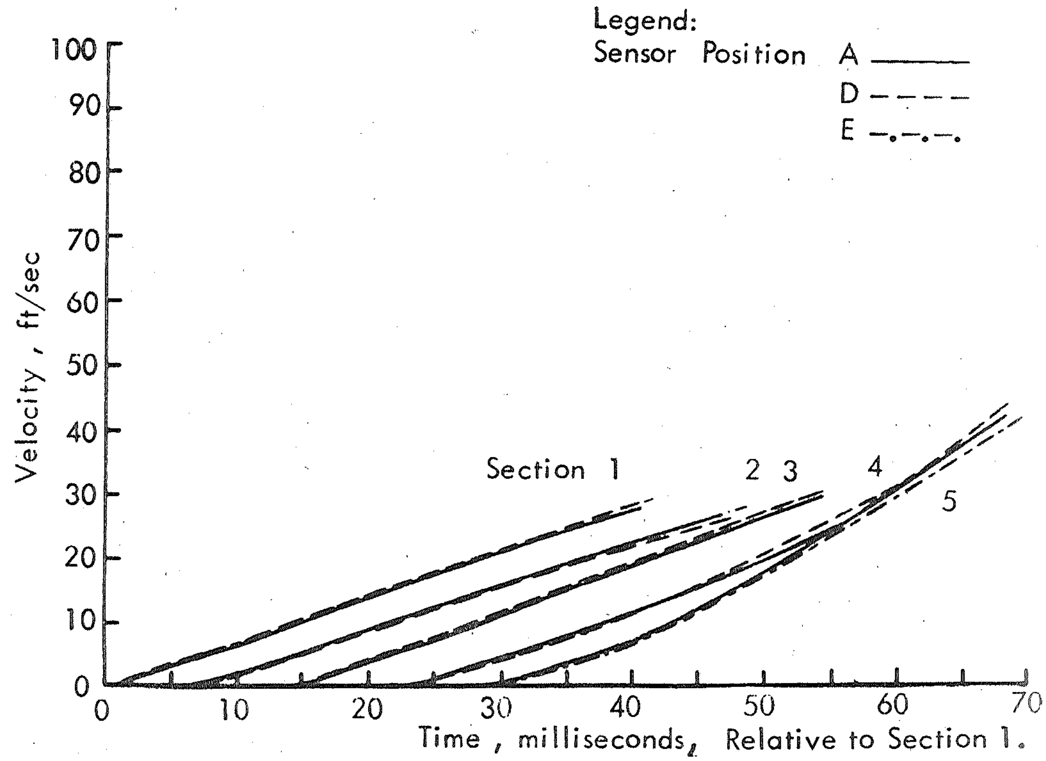

Fig. 14 Flow Velocity Versus Time for Various Sensor Positions at Diaphragm Burst Pressure of 20 psi.

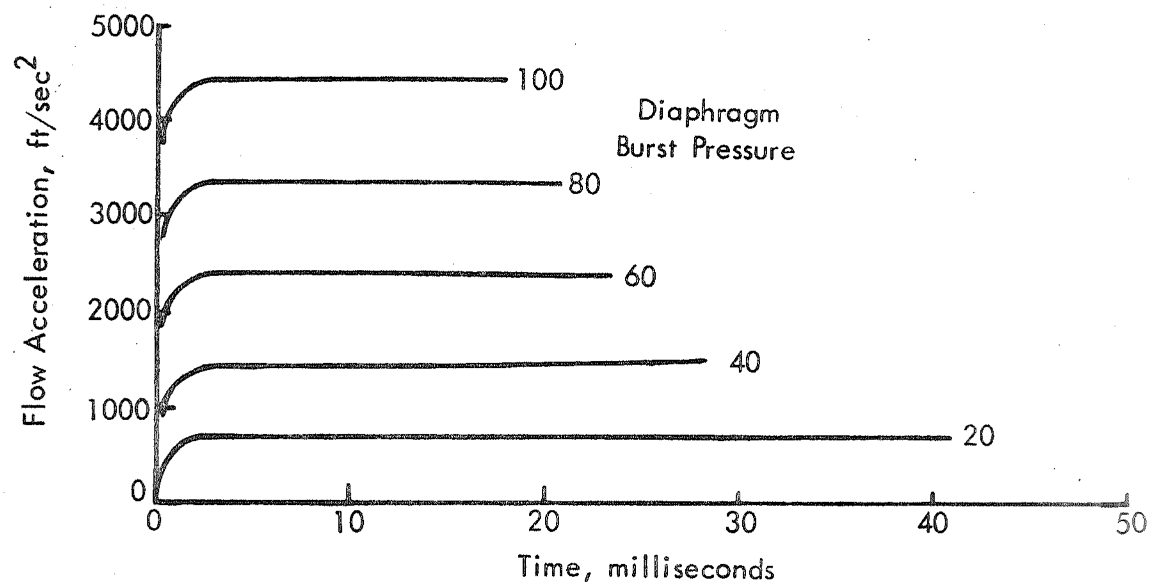

Fig. 15 Flow Acceleration Versus Time for Section 1 and Sensor Position A.

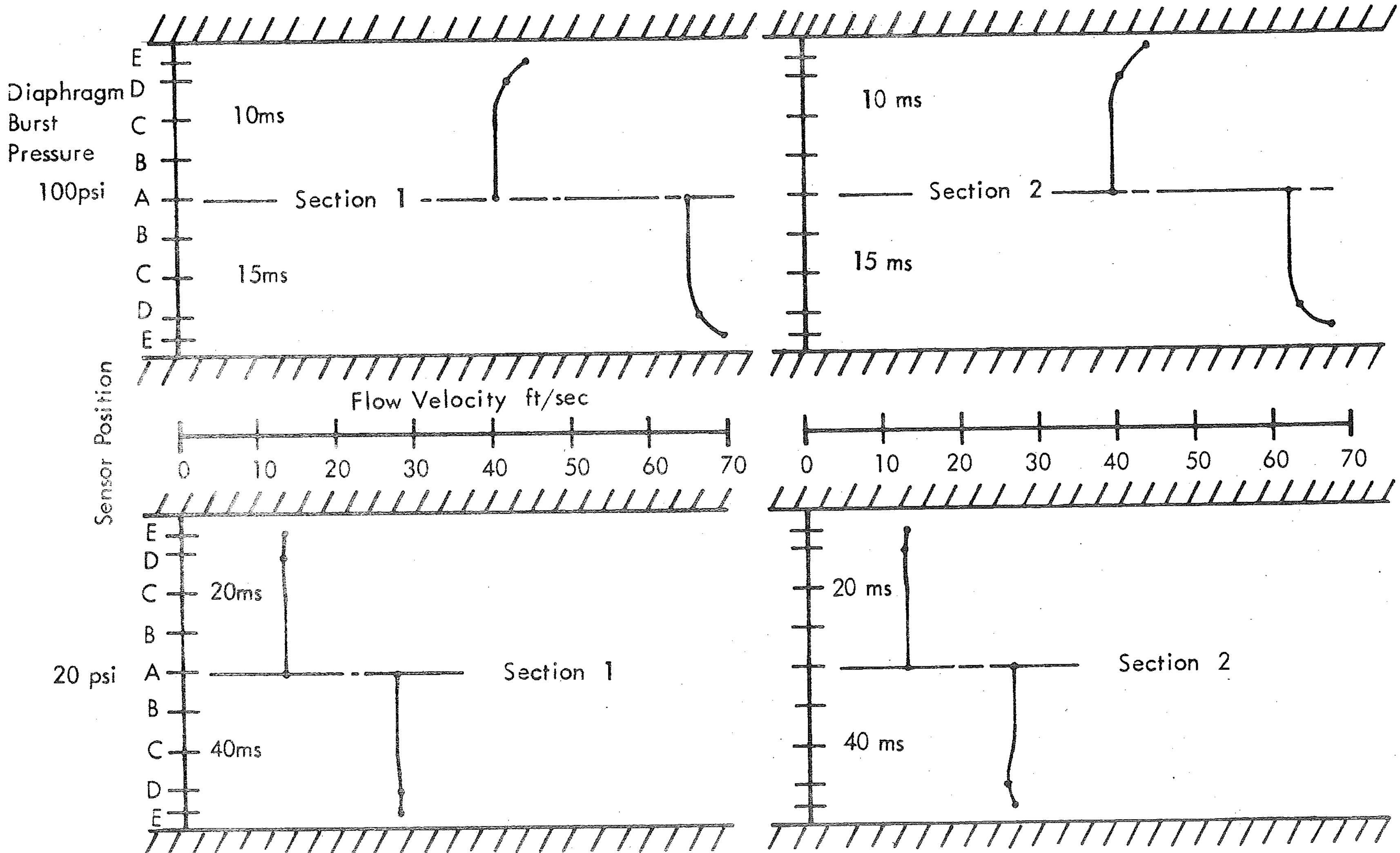

Fig. 16 Velocity Profiles at 2 Time Frames in 2 Pipe Sections for Diaphragm Burst Pressures of 100 psi and 20 psi.

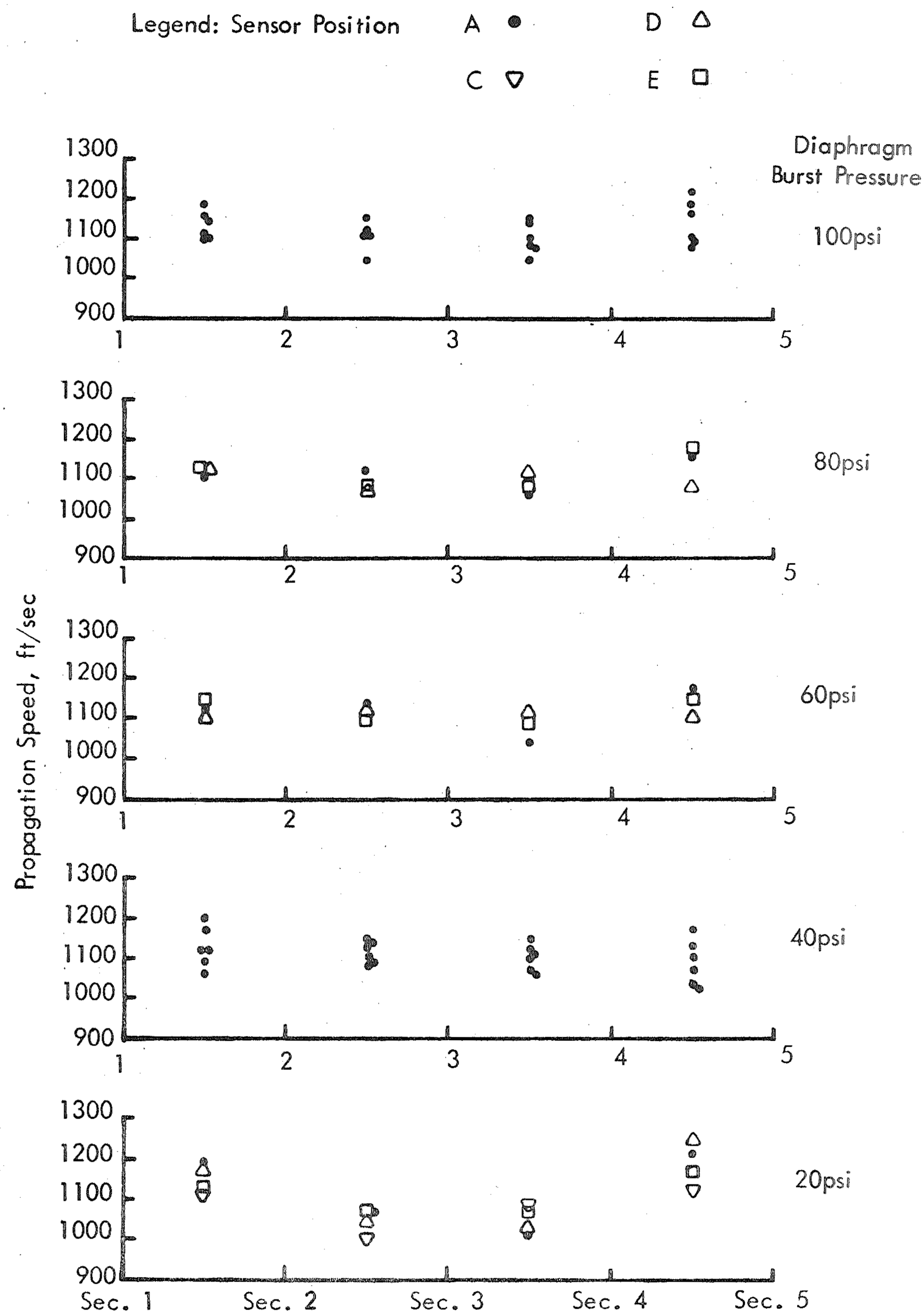

Fig. 17 Propagation Speed of Pressure Wave Versus Axial Distance along Pipe.

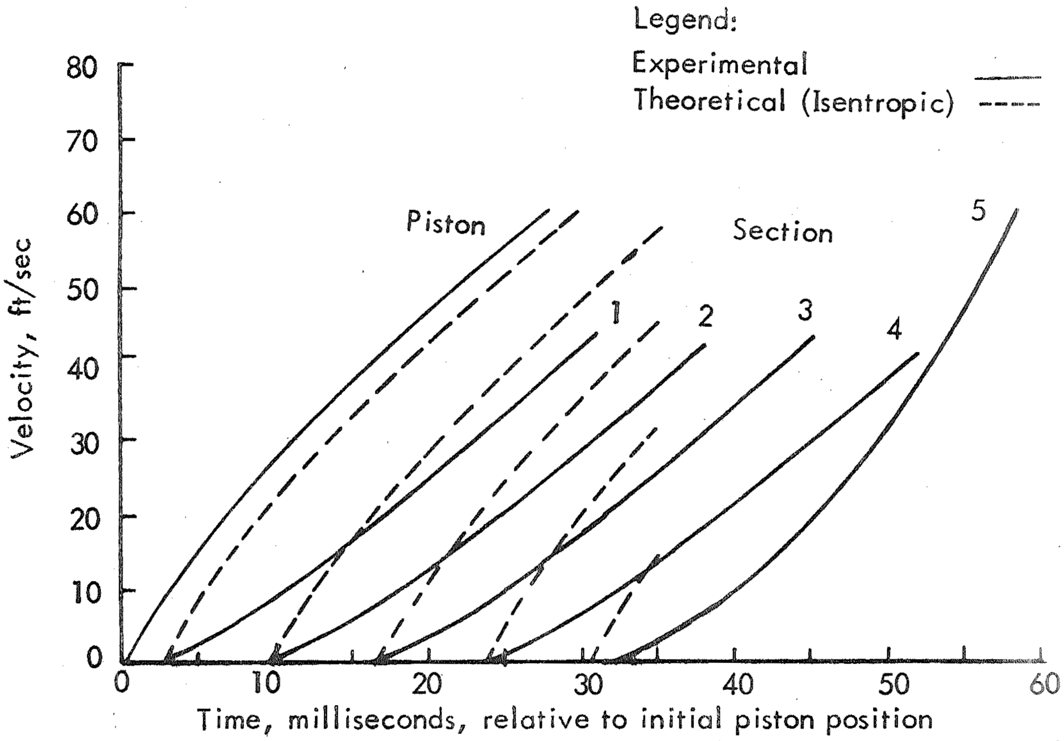

Fig. 18 Comparison of Numerical Calculations with Experimental Data. Burst Pressure 40 psi, Sensor Position A.

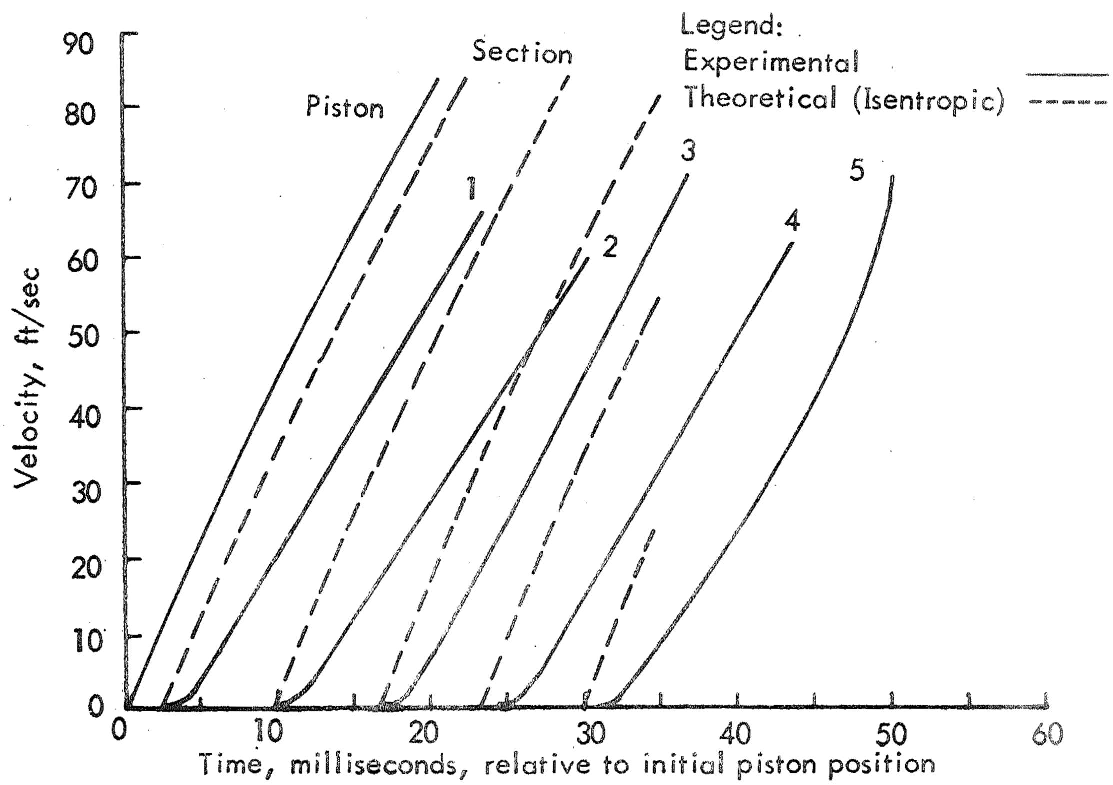

Fig. 19 Comparison of Numerical Calculations with Experimental Data. Burst Pressure 80 psi, Sensor Position A.

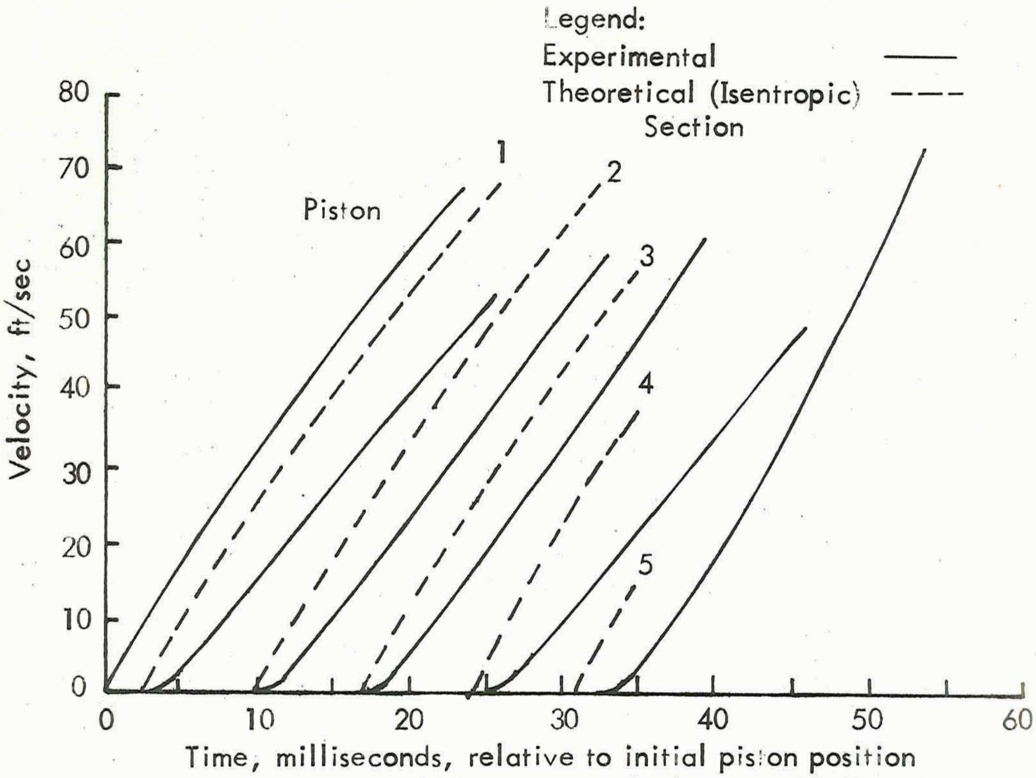

Fig. 20 Comparison of Numerical Calculations with Experimental Data. Burst Pressure 60 psi, Sensor Position A.

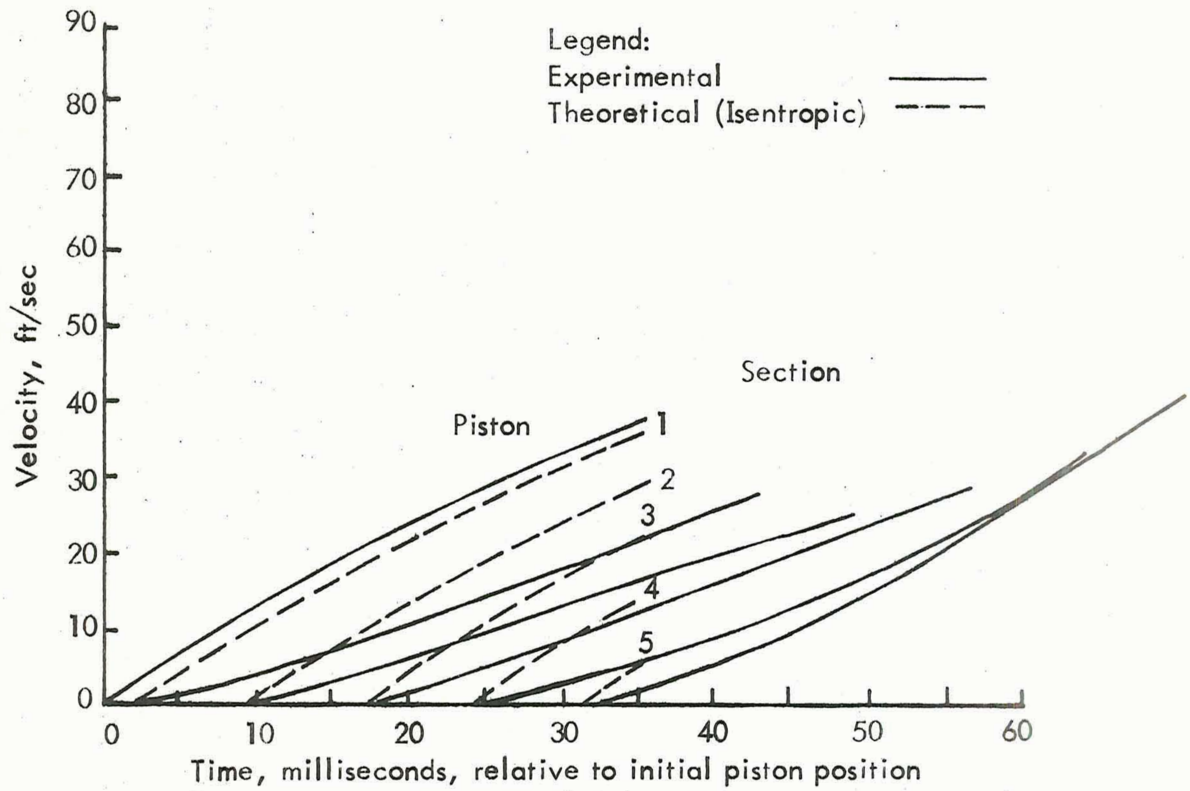

Fig. 21 Comparison of Numerical Calculations with Experimental Data. Burst Pressure 20 psi, Sensor Position A.

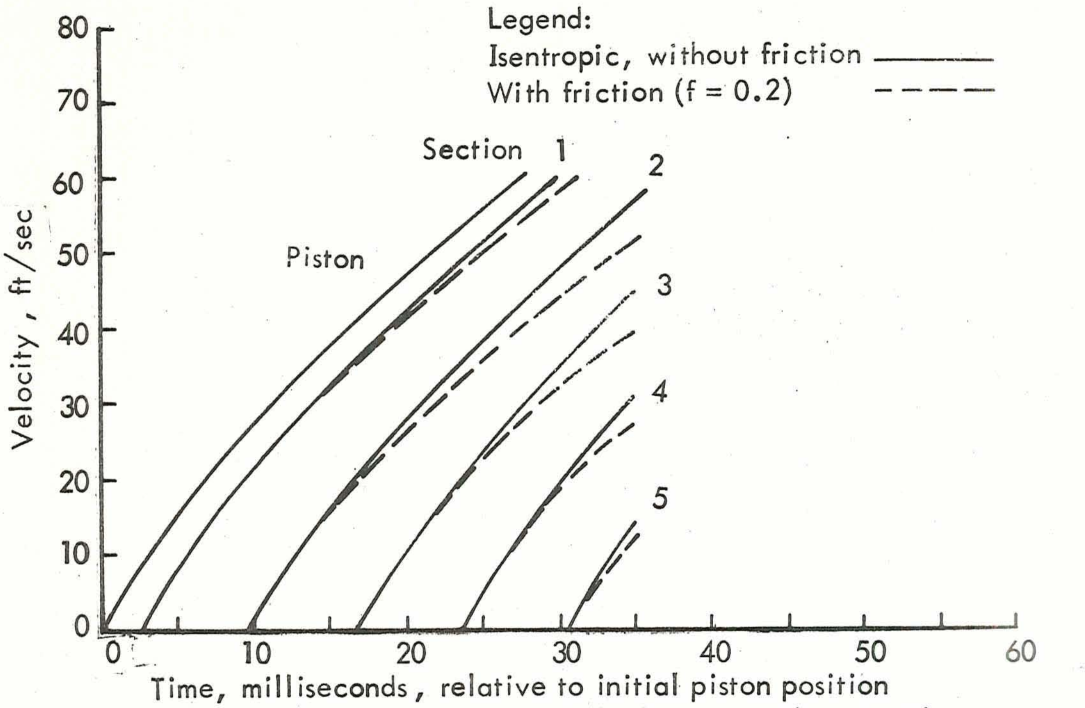

Fig. 22 Comparison of Numerical Calculations with and without Friction (f =0.2) at Burst Pressure 40 psi and Sensor Position A.

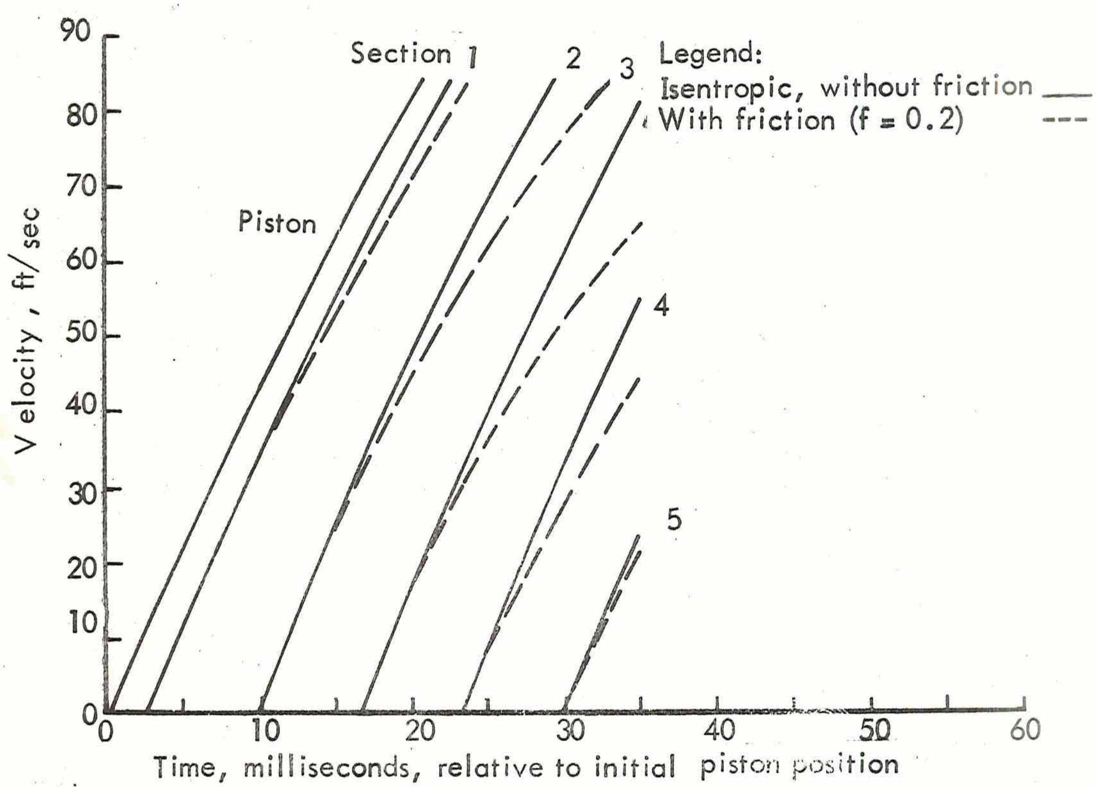

Fig. 23 Comparison of Numerical Calculations with and without Friction (f=0.2) at Burst Pressure 80 psi and Sensor Position A.

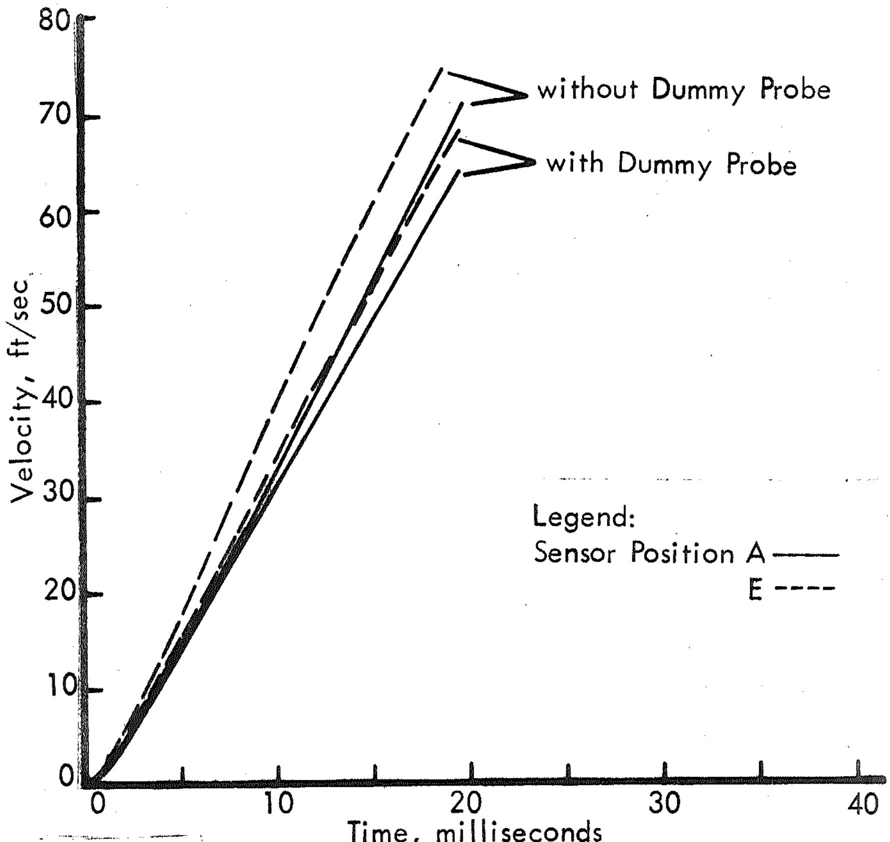

Fig. 24 Study of Blockage Effect - Comparison of Measurements with and without Dummy Probe, at A and E - Position for Burst Pressure of 80 psi.

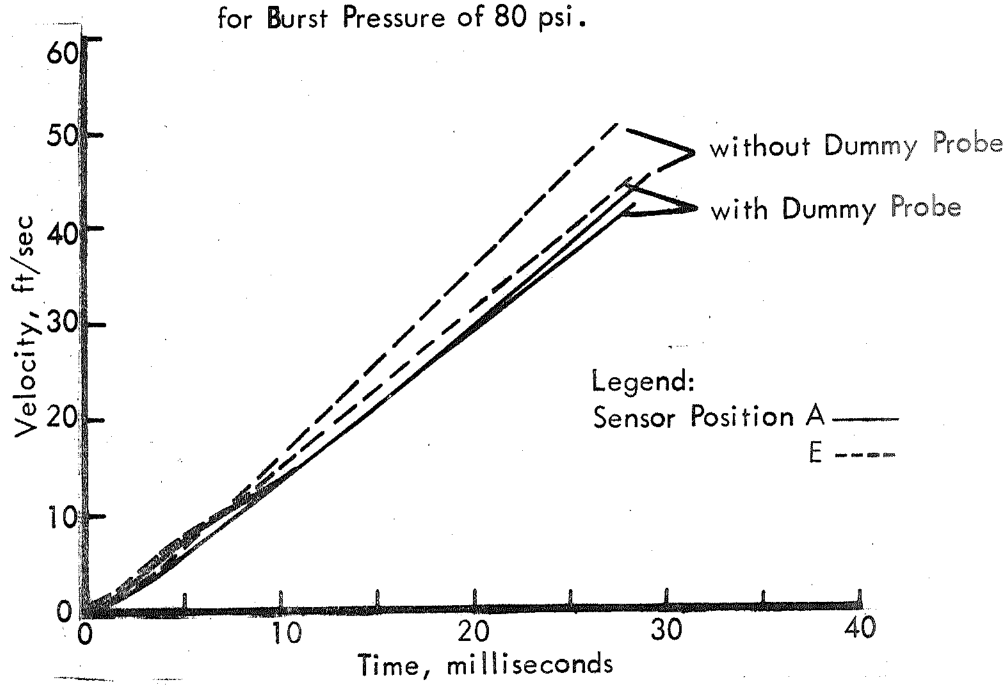

Fig. 25 Study of Blockage Effect — Comparison of Measurements with and without Dummy Probe, at A and E - Position for Burst Pressure of 40 psi.

APPENDIX A

I. LISTING OF COMPUTER PROGRAM FOR BURST PRESSURE 80 PSI, WITHOUT FRICTION

```
      DIMENSION V(101,101),A(101,101),VP(101),AP(101),X(101),T(101)
     1,DT(101),TT(101,101),TP(101)
      READ(5,1000)GAMMA,P0,RHO0,PL,ITMAX,N,C1,C2,C3,C4,C5,D1,D2,D3,D4,D5
      C=P0/(RHO0**GAMMA)
      TEMP=SQRT(1.4*(RHO0**0.4)*C)
      N1=N+1
      RN=N
      DX=PL/RN
      DT(2)=DX/TEMP
      X(1)=0.0
      T(1)=0.0
      DO 10 K=1,ITMAX
      DO 10 J=1,N1
      V(J,K) = 0.0
      A(J,K) = TEMP
   10 CONTINUE
      DO 15 J=1,N1
      VP(J) = 0.0
      TP(J)=0.0
      AP(J) = TEMP
      X(J) = (J-1)*DX
   15 CONTINUE
      K=1
      RHO = RHO0
      WRITE (6,1005) K
      WRITE (6,1010) T(1),RHO
      WRITE (6,1015) (J,X(J),TP(J),VP(J),AP(J),J=1,N1)
      CONST1 = 1.0/(GAMMA-1.0)
      CONST2 = (GAMMA-1.0)/4.0
      DO 40 K=2,ITMAX
      KM1 = K-1
      DO 20 J=1,N
      TT(101,KM1)=TP(101)
      TT(J,KM1)=TP(J)
      V(J,KM1) = VP(J)
      A(J,KM1) = AP(J)
   20 CONTINUE
      TF=T(K-1)+DT(2)
      W=5.86*(TF*1000.)**0.883
      Y=0.2*(W-V(2,KM1))+A(2,KM1)
      DDT=(X(1)-X(2))*2.0/(V(2,KM1)+W-A(2,KM1)-Y)
      TS=T(K-1)+DDT
      WW=5.86*(TS*1000.)**0.883
      YY=0.2*(WW-V(2,KM1))+A(2,KM1)
      DDD=(X(1)-X(2))*2.0/(V(2,KM1)+WW-A(2,KM1)-YY)
      T(K)=T(K-1)+DDD
      VP(1)=5.86*(T(K)*1000.)**0.883
```

```
      AP(1)=0.2*(VP(1)-V(2,KM1))+A(2,KM1)
      DO 30 JJ=2,N
      JJM = JJ-1
      JJP = JJ+1
      VP(JJ) = 0.5*(V(JJM,KM1)+V(JJP,KM1)) + CONST1*(A(JJM,KM1)
     *-A(JJP,KM1))
      AP(JJ) = CONST2*(V(JJM,KM1)-V(JJP,KM1) +
     *2.0*CONST1*(A(JJM,KM1)+A(JJP,KM1)))
      Q=AP(JJ)*(TT(JJP,KM1)-TT(JJM,KM1))+2.0*(X(JJP)-X(JJM))
      S=(TT(JJP,KM1)-TT(JJM,KM1))*(V(JJP,KM1)+VP(JJ)-A(JJP,KM1))
      Z=2.0*AP(JJ)+V(JJM,KM1)+A(JJM,KM1)-V(JJP,KM1)+A(JJP,KM1)
      DT(JJ)=(Q-S)/Z
      TP(JJ)=TT(JJM,KM1)+DT(JJ)
      DX=DT(JJ)*(V(JJM,KM1)+VP(JJ)+A(JJM,KM1)+AP(JJ))/2.0
      X(JJ) = X(JJM) + DX
      TP(1)=T(K)
   30 CONTINUE
      TP(101)=TP(100)
      WRITE(6,1005) K
      WRITE(6,1010) T(K),RHO
      WRITE(6,1006)
      WRITE (6,1015) (J,X(J),TP(J),VP(J),AP(J),J=1,N1)
   40 CONTINUE
 1000 FORMAT(4F10.6,2I5/5E15.8/5E15.8)
 1005 FORMAT('1FOR K =',I3/1H0,'T =',19X,'RHO =')
 1006 FORMAT(1H0,3X,'J',6X,'X(J)',10X,'TP(J)',10X,'VP(J)',10X,'AP(J)')
 1010 FORMAT(1H+,4X,E15.8,9X,E15.8)
 1015 FORMAT(1H ,I4,4E15.8)
      STOP
      END
```

APPENDIX A

II. LISTING OF COMPUTER PROGRAM FOR BURST PRESSURE 80 PSI, WITH FRICTION (f = 0.2)

```
      DIMENSION V(101,101),A(101,101),VP(101),AP(101),X(101),T(101)
     1,DT(101),TT(101,101),TP(101)
      READ(5,1000)GAMMA,P0,RHO0,PL,ITMAX,N,C1,C2,C3,C4,C5,D1,D2,D3,D4,D5
      C=P0/(RHO0**GAMMA)
      TEMP=SQRT(1.4*(RHO0**0.4)*C)
      N1=N+1
      RN=N
      DX=PL/RN
      DT(2)=DX/TEMP
      X(1)=0.0
      T(1)=0.0
      DO 10 K=1,ITMAX
      DO 10 J=1,N1
      V(J,K) = 0.0
      A(J,K) = TEMP
   10 CONTINUE
      DO 15 J=1,N1
      VP(J) = 0.0
      TP(J)=0.0
      AP(J) = TEMP
      X(J) = (J-1)*DX
   15 CONTINUE
      K=1
      RHO = RHO0
      WRITE (6,1005) K
      WRITE (6,1010) T(1),RHO
      WRITE (6,1015) (J,X(J),TP(J),VP(J),AP(J),J=1,N1)
      CONST1 = 1.0/(GAMMA-1.0)
      CONST2 = (GAMMA-1.0)/4.0
      DO 40 K=2,ITMAX
      KM1 = K-1
      DO 20 J=1,N
      TT(101,KM1)=TP(101)
      TT(J,KM1)=TP(J)
      V(J,KM1) = VP(J)
      A(J,KM1) = AP(J)
   20 CONTINUE
      TF=T(K-1)+DT(2)
      W=5.86*(TF*1000.)**0.883
      Y=0.2*(W-V(2,KM1))+A(2,KM1)
      DDT=(X(1)-X(2))*2.0/(V(2,KM1)+W-A(2,KM1)-Y)
      TS=T(K-1)+DDT
      WW=5.86*(TS*1000.)**0.883
      YY=0.2*(WW-V(2,KM1))+A(2,KM1)
      DDD=(X(1)-X(2))*2.0/(V(2,KM1)+WW-A(2,KM1)-YY)
      T(K)=T(K-1)+DDD
      VP(1)=5.86*(T(K)*1000.)**0.883
      AP(1)=0.2*(VP(1)-V(2,KM1))+A(2,KM1)
      DO 30 JJ=2,N
```

```
      JJM = JJ-1
      JJP = JJ+1
      CONST3=FRIC*DT(JJ)/4.0/DIAM
      FRIC=0.2
      DIAM=0.25
      CONST4=CONST3*(GAMMA-1.0)/2.0
      VP(JJ) = 0.5*(V(JJM,KM1)+V(JJP,KM1)) + CONST1*(A(JJM,KM1)
     *-A(JJP,KM1))
     *-CONST3*(V(JJM,KM1)*ABS(V(JJM,KM1))+V(JJP,KM1)*ABS(V(JJP,KM1)))
      AP(JJ) = CONST2*(V(JJM,KM1)-V(JJP,KM1) +
     *2.0*CONST1*(A(JJM,KM1)+A(JJP,KM1)))
     *+CONST4*(V(JJP,KM1)*ABS(V(JJP,KM1))-V(JJM,KM1)*ABS(V(JJM,KM1)))
      Q=AP(JJ)*(TT(JJP,KM1)-TT(JJM,KM1))+2.0*(X(JJP)-X(JJM))
      S=(TT(JJP,KM1)-TT(JJM,KM1))*(V(JJP,KM1)+VP(JJ)-A(JJP,KM1))
      Z=2.0*AP(JJ)+V(JJM,KM1)+A(JJM,KM1)-V(JJP,KM1)+A(JJP,KM1)
      DT(JJ)=(Q-S)/Z
      TP(JJ)=TT(JJM,KM1)+DT(JJ)
      DX=DT(JJ)*(V(JJM,KM1)+VP(JJ)+A(JJM,KM1)+AP(JJ))/2.0
      X(JJ) = X(JJM) + DX
      TP(1)=T(K)
   30 CONTINUE
      TP(101)=TP(100)
      WRITE(6,1005) K
      WRITE(6,1010) T(K),RHO
      WRITE(6,1006)
      WRITE (6,1015) (J,X(J),TP(J),VP(J),AP(J),J=1,N1)
   40 CONTINUE
 1000 FORMAT(4F10.6,2I5/5E15.8/5E15.8)
 1005 FORMAT('1FOR K =',I3/1H0,'T =',19X,'RHO =')
 1006 FORMAT(1H0,3X,'J',6X,'X(J)',10X,'TP(J)',10X,'VP(J)',10X,'AP(J)')
 1010 FORMAT(1H+,4X,E15.8,9X,E15.8)
 1015 FORMAT(1H ,I4,4E15.8)
      STOP
      END
```

APPENDIX B

TABULATED DATA

DATA SHEET NO. 1	TIME MS	SEC 1 VEL FT/SEC	SEC 2 VEL FT/SEC	SEC 3 VEL FT/SEC	SEC 4 VEL FT/SEC	SEC 5 VEL FT/SEC
FIG. 8	1.0	1.1	1.2	1.0	.9	1.0
100 PSI	2.0	4.1	5.0	5.1	4.6	4.3
S.P. A	3.0	7.9	8.3	9.5	8.9	9.1
TEST	5.0	17.1	16.9	18.4	18.1	18.7
81,83,85	7.0	25.3	26.4	28.4	27.2	28.6
Average	10.0	39.3	40.7	43.5	41.3	41.4
Values	15.0	62.6	61.0	67.2	65.3	70.3
	18.1	76.2				
	17.5		71.8			
	17.0			77.7		
	16.3				73.0	
	15.8					78.5

DELTA T = 7.2, 7.2, 7.4, 7.1 MILLISECONDS

FIG. 8	1.0	.3	.4	.4	.3	.4
40 PSI	2.0	1.0	1.2	1.3	.9	1.3
S.P. A	3.0	2.3	2.7	2.8	2.1	2.6
TEST	5.0	5.1	5.4	5.6	5.1	5.4
78,82,84	7.0	8.4	8.3	8.7	8.2	8.4
Average	10.0	12.7	12.3	13.0	12.3	12.1
Values	15.0	20.4	19.3	20.8	19.8	21.9
	20.0	28.0	27.4	29.1	27.3	36.4
	25.0	36.4	35.3	38.1	35.4	51.3
	28.9	43.7				
	28.7		42.0			
	28.5			43.7		
	27.9				40.9	
	27.5					60.1

DELTA T = 7.2, 7.3, 7.3, 7.4 MILLISECONDS

DATA SHEET NO. 2	TIME MS	SEC 1 VEL FT/SEC	SEC 2 VEL FT/SEC	SEC 3 VEL FT/SEC	SEC 4 VEL FT/SEC	SEC 5 VEL FT/SEC
FIG. 9	1.0	.3	.5	.5	.3	.4
40 PSI	2.0	1.0	1.9	1.6	.9	1.4
S.P. A	3.0	2.0	3.3	2.9	2.4	2.9
TEST 86	5.0	4.6	5.9	5.4	5.3	5.8
	7.0	8.3	9.1	9.1	8.5	9.4
	10.0	13.4	12.9	14.3	12.9	13.1
	15.0	21.3	19.5	21.4	20.1	24.0
	20.0	29.6	27.6	29.3	28.4	40.2
	25.0	38.5	35.1	38.0	36.5	55.7
	28.6	45.0				
	28.3		38.5			
	28.1			43.0		
	27.9				41.7	
	27.2					61.5

DELTA T = 7.2, 7.1, 6.9, 7.7 MILLISECONDS

FIG. 9	1.0	.4	.5	.5
40 PSI	2.0	1.0	1.5	1.5
S.P. A	3.0	2.4	3.2	3.1
TEST 87	5.0	5.1	5.9	7.3
	7.0	8.9	9.1	14.0
	10.0	13.6	13.3	22.4
	15.0	21.7	21.0	41.9
	20.0	31.0	30.2	60.4
	25.0	39.4	44.9	76.6
	28.3	44.0		
	28.2		52.7	
	27.6			84.0

DELTA T = 7.1, 7.2, MILLISECONDS

DATA SHEET NO. 3	TIME MS	SEC 1 VEL FT/SEC	SEC 2 VEL FT/SEC	SEC 3 VEL FT/SEC	SEC 4 VEL FT/SEC	SEC 5 VEL FT/SEC
FIG. 10	1.0	1.1	1.0	1.1	.9	1.4
100 PSI	2.0	4.5	4.7	5.6	4.1	5.1
S.P. A	3.0	9.0	5.8	10.4	8.5	9.6
TEST 81	5.0	18.0	17.3	19.5	18.2	17.7
	7.0	26.5	26.2	31.1	28.0	27.5
	10.0	42.0	41.0	47.5	40.0	39.0
	15.0	65.2	61.7	72.0	67.5	63.0
	18.3	80.5				
	17.7		73.0			
	17.1			85.0		
	16.3				75.0	
	16.0					73.5

DELTA T = 7.3, 7.3, 7.7, 6.8 MILLISECONDS

FIG. 10	1.0	1.7	.8	1.3	.7	1.3
100 PSI	2.0	6.0	5.4	5.3	4.0	6.2
S.P. D	3.0	9.7	9.0	10.1	8.2	10.1
TEST 70	5.0	19.5	17.8	19.7	18.0	17.7
	7.0	27.7	27.0	32.0	27.2	27.2
	10.0	42.5	40.5	47.5	40.0	39.5
	15.0	66.5	61.8	71.5	68.0	65.5
	18.0	79.5				
	17.5		74.0			
	17.2			83.0		
	16.4				73.2	
	16.1					73.5

DELTA T = 7.2, 7.0, 7.4, 7.0 MILLISECONDS

DATA SHEET NO. 4	TIME MS	SEC 1 VEL FT/SEC	SEC 2 VEL FT/SEC	SEC 3 VEL FT/SEC	SEC 4 VEL FT/SEC	SEC 5 VEL FT/SEC
FIG. 10	1.0	1.3	1.2	1.7	1.0	1.2
100 PSI	2.0	5.5	6.3	7.2	4.2	5.9
S.P. E	3.0	10.5	10.8	11.8	9.2	10.5
TEST 75	5.0	20.2	20.2	23.2	20.0	19.3
	7.0	30.5	29.5	35.0	29.8	29.5
	10.0	46.3	43.7	51.5	46.3	42.5
	15.0	71.2	66.0	78.0	74.5	69.8
	17.2	79.5				
	17.3		79.5			
	16.7			90.0		
	16.0				79.5	
	15.7					76.0

DELTA T = 7.2, 7.3, 7.3, 7.0 MILLISECONDS

FIG. 11	1.0	.6	.5	.6	.7	.9
80 PSI	2.0	3.2	2.9	3.0	2.6	3.9
S.P. A	3.0	6.0	6.0	6.6	5.8	6.7
TEST 80	5.0	12.5	11.0	13.3	12.3	12.5
	7.0	19.0	18.5	19.7	19.7	18.3
	10.0	27.5	27.5	31.8	28.0	27.2
	15.0	46.0	43.0	51.0	46.3	46.5
	20.0	63.5	59.0	.0	.0	.0
	21.2	66.5				
	20.5		60.0			
	20.0			71.2		
	19.2				62.0	
	19.2					71.5

DELTA T = 7.3, 7.0, 7.6, 6.8 MILLISECONDS

DATA SHEET NO. 5	TIME MS	SEC 1 VEL FT/SEC	SEC 2 VEL FT/SEC	SEC 3 VEL FT/SEC	SEC 4 VEL FT/SEC	SEC 5 VEL FT/SEC
FIG. 11	1.0	.9	.6	1.2	.5	1.5
80 PSI	2.0	3.7	3.6	4.5	2.3	4.5
S.P. D	3.0	7.0	7.2	8.0	5.0	7.6
TEST 69	5.0	14.5	13.1	15.0	12.5	13.5
	7.0	20.0	20.0	23.5	19.5	20.0
	10.0	32.5	30.0	33.3	30.0	29.5
	15.0	50.0	46.3	55.5	49.0	49.5
	20.3	70.8				
	19.7		62.5			
	19.1			68.5		
	18.9				63.0	
	18.2					68.0

DELTA T = 7.1, 7.4, 7.2, 7.3 MILLISECONDS

FIG. 11	1.0	1.2	.6	1.4	.7	.9
80 PSI	2.0	4.5	3.5	5.0	3.3	4.0
S.P. E	3.0	7.9	7.8	8.5	7.4	7.6
TEST 74	5.0	15.7	14.5	16.7	15.2	14.5
	7.0	22.5	22.2	25.9	22.8	21.3
	10.0	34.9	34.0	38.7	32.7	31.0
	15.0	55.5	52.0	60.3	54.0	52.0
	19.3	71.0				
	19.3		69.0			
	18.9			75.0		
	18.2				68.9	
	18.3					73.0

DELTA T = 7.1, 7.4, 7.3, 7.0 MILLISECONDS

DATA SHEET NO. 6	TIME MS	SEC 1 VEL FT/SEC	SEC 2 VEL FT/SEC	SEC 3 VEL FT/SEC	SEC 4 VEL FT/SEC	SEC 5 VEL FT/SEC
FIG. 12	1.0	.5	.7	.3	.3	.3
60 PSI	2.0	1.5	1.9	2.2	1.0	.6
S.P. A	3.0	4.4	4.6	5.6	2.8	2.1
TEST 49	5.0	9.9	10.7	11.3	7.7	7.2
	7.0	15.1	14.9	16.1	13.0	12.8
	10.0	21.5	23.0	24.8	20.3	21.0
	15.0	32.5	37.0	39.0	31.7	38.7
	23.6	53.5				
	23.3		59.4			
	22.4			61.9		
	22.2				48.7	
	22.3					72.5

DELTA T = 7.3, 7.4, 7.1, 6.9 MILLISECONDS

FIG. 12	1.0	.5	.6	.9	.5	.9
60 PSI	2.0	2.8	2.4	3.3	1.5	3.3
S.P. D	3.0	5.1	4.8	6.0	4.0	5.7
TEST 66	5.0	10.4	9.7	11.2	9.0	10.2
	7.0	15.5	15.5	17.3	15.0	15.1
	10.0	23.5	22.1	25.5	21.5	21.7
	15.0	37.5	36.7	42.5	36.0	38.0
	20.0	52.5	49.0	56.5	50.0	60.0
	22.8	59.0				
	22.7		55.0			
	22.1			61.5		
	21.8				55.0	
	21.4					65.6

DELTA T = 7.2, 7.1, 7.2, 7.3 MILLISECONDS

DATA SHEET NO. 7	TIME MS	SEC 1 VEL FT/SEC	SEC 2 VEL FT/SEC	SEC 3 VEL FT/SEC	SEC 4 VEL FT/SEC	SEC 5 VEL FT/SEC
FIG. 12	1.0	1.0	.5	1.0	.5	.9
60 PSI	2.0	3.4	3.0	3.5	2.1	3.4
S.P. E	3.0	5.5	5.6	6.2	4.4	5.4
TEST 73	5.0	11.3	10.4	11.6	9.4	10.2
	7.0	16.4	16.0	17.6	15.5	15.6
	10.0	24.3	23.5	26.1	22.8	21.7
	15.0	37.8	37.1	44.0	37.0	36.8
	20.0	52.0	51.2	58.3	50.0	60.0
	22.7	59.7				
	22.8		56.5			
	22.3			62.6		
	21.8				53.7	
	21.7					66.9

DELTA T = 7.1, 7.4, 7.3, 7.0 MILLISECONDS

FIG. 13	1.0	.4	.5	.2	.4	.3
40 PSI	2.0	.9	1.5	1.0	1.0	.9
S.P. A	3.0	2.3	2.9	2.5	2.1	2.0
TEST 82	5.0	5.2	5.5	5.5	5.8	4.9
	7.0	8.5	8.5	8.5	9.0	8.4
	10.0	12.8	13.0	12.5	12.9	12.0
	15.0	20.6	20.2	20.7	20.8	21.5
	20.0	28.2	30.1	28.0	28.5	37.6
	25.0	36.3	38.0	36.4	37.0	55.5
	28.8	42.5				
	28.5		45.9			
	28.1			41.3		
	27.5				41.3	
	27.2					65.0

DELTA T = 7.6, 7.1, 7.6, 7.1 MILLISECONDS

DATA SHEET NO. 8	TIME MS	SEC 1 VEL FT/SEC	SEC 2 VEL FT/SEC	SEC 3 VEL FT/SEC	SEC 4 VEL FT/SEC	SEC 5 VEL FT/SEC
FIG. 13	1.0	.4	.3	.4	.3	.4
40 PSI	2.0	1.3	1.1	1.4	.9	1.6
S.P. D	3.0	2.9	2.4	2.6	2.0	3.1
TEST 67	5.0	5.4	5.2	5.7	4.8	5.7
	7.0	8.4	8.2	9.0	8.4	8.5
	10.0	12.7	12.0	14.2	12.5	12.0
	15.0	20.0	19.5	23.5	20.1	21.4
	20.0	27.6	27.5	32.5	28.5	35.7
	25.0	35.3	35.4	41.0	35.9	49.0
	29.1	44.0				
	28.8		40.9			
	28.7			46.1		
	27.9				40.5	
	27.7					57.0

DELTA T = 7.3, 7.1, 7.6, 7.0 MILLISECONDS

FIG. 13	1.0	.2	.2	.4	.2	.4
40 PSI	2.0	1.4	.6	1.4	.9	1.6
S.P. E	3.0	2.6	2.6	3.4	2.1	3.6
TEST 72	5.0	6.0	5.7	6.6	4.9	5.9
	7.0	9.1	8.9	10.6	8.4	9.4
	10.0	14.5	14.2	15.7	12.6	13.3
	15.0	22.5	22.1	25.5	21.5	23.1
	20.0	32.5	31.5	35.4	29.5	36.5
	25.0	42.7	39.8	44.2	39.7	52.5
	28.7	48.5				
	28.4		46.3			
	27.9			51.0		
	27.5				43.0	
	27.1					59.9

DELTA T = 7.1, 7.4, 7.5, 7.0 MILLISECONDS

DATA SHEET NO. 9	TIME MS	SEC 1 VEL FT/SEC	SEC 2 VEL FT/SEC	SEC 3 VEL FT/SEC	SEC 4 VEL FT/SEC	SEC 5 VEL FT/SEC
FIG. 14	1.0	.3	.2	.4	.3	.3
20 PSI	2.0	.9	.5	.9	.7	.9
S.P. A	3.0	1.6	1.0	1.5	1.4	1.8
TEST 77	5.0	3.3	2.5	3.1	2.6	3.1
	7.0	4.1	3.8	4.4	3.5	4.3
	10.0	5.7	5.6	6.1	5.2	5.9
	15.0	9.5	9.0	10.0	8.5	10.5
	20.0	13.5	12.3	14.5	12.3	16.5
	25.0	17.5	16.2	18.1	16.5	23.0
	30.0	20.5	19.0	22.5	21.2	28.5
	35.0	24.0	22.7	25.7	27.5	35.2
	40.0	27.2	26.0	28.5	.0	.0
	40.7	27.5				
	40.8		26.8			
	40.4			30.0		
	39.4				32.5	
	39.7					42.3

DELTA T = 6.7, 7.5, 7.9, 6.7 MILLISECONDS

FIG. 14	1.0	.3	.2	.4	.3	.4
20 PSI	2.0	.6	.5	.8	.6	.7
S.P. D	3.0	1.5	1.0	1.5	1.3	1.4
TEST 68	5.0	3.0	2.5	3.3	2.6	3.1
	7.0	4.2	3.7	4.6	3.7	4.2
	10.0	5.9	5.6	6.7	5.5	6.0
	15.0	9.3	9.0	10.5	8.7	10.3
	20.0	13.2	12.6	14.5	12.6	16.2
	25.0	16.7	16.3	18.5	17.0	22.1
	30.0	20.2	19.6	22.5	21.6	29.0
	35.0	24.5	22.9	26.7	27.5	35.5
	40.0	27.8	25.5	.0	.0	.0
	40.7	28.6				
	40.7		25.9			
	40.1			30.0		
	39.6				32.7	
	39.9					43.5

DELTA T = 6.9, 7.7, 7.8, 6.4 MILLISECONDS

DATA SHEET NO. 10	TIME MS	SEC 1 VEL FT/SEC	SEC 2 VEL FT/SEC	SEC 3 VEL FT/SEC	SEC 4 VEL FT/SEC	SEC 5 VEL FT/SEC
FIG. 14	1.0	.1	.2	.4	.1	.3
20 PSI	2.0	.6	.5	.9	.5	.7
S.P. E	3.0	1.5	1.1	1.7	1.0	1.5
TEST 71	5.0	2.9	2.7	3.7	2.4	3.0
	7.0	4.1	4.0	4.6	3.5	4.2
	10.0	6.1	6.0	6.6	5.4	5.8
	15.0	9.6	9.3	10.2	9.0	9.8
	20.0	14.2	12.8	14.1	12.5	16.0
	25.0	17.5	16.6	17.6	16.0	21.2
	30.0	20.6	19.2	21.0	21.0	27.5
	35.0	24.5	23.5	25.7	25.5	34.0
	40.0	27.6	26.2	29.0	32.5	39.8
	41.7	28.7				
	41.6		27.3			
	41.3			30.0		
	40.7				34.1	
	40.7					41.2

DELTA T = 7.3, 7.3, 7.5, 6.9 MILLISECONDS

SECTION II

EXPERIMENTAL INVESTIGATION OF EFFECTS OF UNSTEADY FLOWS ON A SUBMERGED CYLINDER

SECTION II

EXPERIMENTAL INVESTIGATION OF EFFECTS OF UNSTEADY FLOWS ON A SUBMERGED CYLINDER

ABSTRACT

Results of investigations of the unsteady flow phenomena about a submerged right circular cylinder are presented. This experimentation was conducted in accelerating flows of from zero to 32 ft/sec^2 using the Unsteady Hydrodynamic Flow Facility of the Fluid Dynamics Laboratory, The University of Alabama in Huntsville, Huntsville, Alabama.

A set of dimensionless parameters consisting of quantities pertinent to the unsteady flows is used to analyze pressure and force data which are presented in terms of local pressure coefficients, lift and drag coefficients versus instantaneous Reynolds number and nondimensional fluid displacement respectively. The measured drag coefficients were found to be comparable with the calculated ones from the pressure coefficients.

A variation of the hydrogen bubble technique was used in obtaining high speed movies of the unsteady flow phenomena about the circular cylinder. A sequence of photographs taken from these movies is presented which shows the development of the flow field around the cylinder at various times.

INTRODUCTION

As rocket technology advanced with its larger and larger launch vehicles, the influence of the unsteady ground winds on vehicle development began to draw considerable interest of the fluid dynamisist. In June of 1966, a National Aeronautics and Space Administration (NASA) sponsored symposium on ground winds[1] reported that there are two items of research importance: 1) basic research into time-dependent flows about a circular cylinder, and 2) better definition of time varying atmospheric characteristics at the launch sites.

The seriousness of the ground winds problem stems from the fact that launch vehicles loads induced by these winds can result in (a) heavier launch vehicles, (b) requirement for a launch vehicle structural response damping system and (c) launch schedule slippage. If the loads imposed by the ground winds were predictable, their effects could be assessed early in the design phases of vehicle development. Currently, the best engineering technique available for estimating the unsteady wind loads requires the aeroelastic model testing of the launch vehicle. In these aeroelastic tests, the structural response of elastically scaled models is determined for steady-wind conditions with these results then being scaled to full-scale vehicle conditions for engineering loads estimation. This type of testing yields engineering data for many types of important physically realizable wind conditions where the wind velocity is constant.

The flow field about a circular cylinder resulting from a steady approaching flow has been studied by many investigators since the cylinder represents the simplest of all bluff bodies, but few studies have been conducted on the flow field resulting from an unsteady approaching flow. Although the past three years has seen an influx of information in this area, it is far from complete for establishing a theory of unsteady flow phenomena about submerged bodies.

This paper presents some results of two series of investigations into the complex phenomena associated with the time-dependent flow about a circular cylinder. The eventual objective of these investigations is to determine the statistical description of the aerodynamic forcing functions for application to elastic bodies submerged in unsteady flow. Since the phenomena of interest occur at low Mach numbers where compressibility is negligibly small, the dynamic similarity between the phenomena with air and water justifies the use of an unsteady hydrodynamic flow facility for the study.

DESCRIPTION OF THE TEST FACILITY

The test facility used in this study was developed at the Fluid Dynamics Laboratory of The University of Alabama in Huntsville. Complete details of its development can be found in Schutzenhofer's work[a]. The facility consists of a water tunnel with a quick start mechanism and various instrumentation systems for the determination of velocity, pressure, and lift and drag forces. A general view and a schematic of the facility are shown in Figure 1.

The water tunnel is a vertically erected steel tank 21.13 feet in length and 2.83 feet in diameter. Two chordwise flow straighteners running the entire tank length help to provide two dimensional flow, but at the same time reduce the useful test section to 1.96 feet. Plexiglass windows set into the flow straighteners allow the model ends to be built in to reduce the undesirable end effects. These windows also allow high speed movies of the flow field around the model to be taken. The test models currently in use are right circular cylinders with an outside diameter of 3.00 inches and are installed perpendicular to the windows.

Quick start of the flow is achieved by thermally rupturing a 0.0014 inch thick mylar diaphragm located at the tank bottom. At the test section of the facility, water flows with acceleration levels of up to 32 ft/sec^2 can be produced by varying the opening area of the diaphragm. The instantaneous velocities of various locations in the test section have been checked using a constant temperature anemometer and show maximum variations of about ten percent.

The arrangement of the water tunnel allows a unique variation of the hydrogen bubble technique to be applied. Electrolysis of the water contained in the tunnel is achieved by passing a continuous dc voltage between a 0.003 inch diameter steel wire and a large copper bar located at the tank bottom. When the hydrogen bubbles first generated have risen to the surface thereby seeding the entire tunnel, the flow is started. This differs from the common usage of the hydrogen bubble technique in that the bubbles are in the flow as it starts rather than being swept by the flow from a wire as they are generated.

INSTRUMENTATION AND DATA REDUCTION

For simplicity and economy, a cantilevered strain gage balance system was found to best meet all the criteria of a measurement system of hydrodynamic forces; namely, the determination of the instantaneous lift and drag forces acting on the full cylinder length. Because of the desirability of having the natural frequency of the cantilevered system approximately five times higher than the estimated frequency of the unsteady forces, it was necessary to consider the balance/cylinder combination as a unit. This was complicated by the addition of six pounds (at maximum acceleration) of virtual mass which acts with the cylinder mass because of the accelerating flow. By performing a parametric dynamic analysis of the balance/cylinder combination, the lengths and cross sections of the balance and cylinder sections were defined to yield a natural frequency of about 200 Hertz while producing a reasonably high sensitivity. This analysis revealed that a built-up cylinder model of stainless steel and aluminum would best meet the established cirteria. Details of this system are given in Morrow's work[3].

The surface pressures on the cylinder model were measured with flush-mounted Kistler pressure transducers. The pressure data were electronically low-pass filtered with the cut-off frequency of 20 Hz. discriminating the pressure waves due to the water hammer created by the rapid opening of the exit area.

A digital data reduction system consisting of a wide band analog recorder, an analog to digital converter and a third generation digital computer (UNIVAC 1108) has been established to aid in the analysis of the data. Foremost in the digital software associated with the data reduction system has been a low-pass filter constructed by using the Fast Fourier Transform technique.

FLOW VISUALIZATION

A sequence of photographs taken from a movie film showing a typical unsteady flow field is presented in Figure 2. This sequence was taken from a film shot at 400 frames/second of the case for which pressure and force data have been presented. Part (a) shows the initial pair of vortices as they break away from the cylinder. Parts (b), (c), and (d) show the breakdown of the wake structure as the Reynolds number increases.

PRESSURE DATA

The pressure coefficient data presented on Figure 3 are the low frequency components of the pressure field, ranging from 0 to 20 Hz. These unsteady pressure data were acquired in an unsteady velocity field that has a constant acceleration of about 32.2 ft/sec^2. For unsteady flow, the pressure coefficient has been defined in [2] as

$$C_P = \frac{P_B - (P_{S\infty} - 1/2\ \rho_0 U^2)}{P_{BFS} - (P_{S\infty} - 1/2\ \rho_0 U^2)} \qquad (1)$$

where P_{BFS} is the pressure at the forward stagnation point on the submerged body, $P_{S\infty}$ is the stagnation pressure at infinity, ρ_0 is the density and U is the velocity at infinity. This method of nondimensionalization appears to have advantages as compared to other methods. With this form, C_P is independent of $(P_{S\infty} - \frac{1}{2}\rho_0 U^2)$, remains finite, has a value of unity at the forward stagnation point, and can be applied to steady and unsteady flow phenomena.

The pressure coefficient at various angular coordinates is presented as a function of nondimensional fluid displacement $(Z_0 - Z_1)/D$, where $(Z_0 - Z_1)$ is the fluid displacement and D is the diameter of the submerged cylinder. In this figure, $\theta = 0$ corresponds to the rear stagnation point. Shown also on Figure 3 are the values of the steady pressure coefficient as taken from Schlichting[4] and values of the unsteady pressure coefficient resulting from unsteady potential theory calculations. The unsteady pressure coefficient data obtained with Equation (1) can be compared to the steady pressure coefficient data since

$$P_{BFS} - (P_{S\infty} - 1/2\ \rho_0 U^2)$$

is not significantly different in numerical value than $\frac{1}{2}\rho_0 U^2$ for $(Z_0 - Z_1)/D \geqq 5.0$.

Except for some oscillations that occur for $0 \leqq (Z_0 - Z_1)/D < 2.5$, C_P is a smooth function of $(Z_0 - Z_1)/D$ and compares favorably with the data in [4] at the same Reynolds number. The exception to this comparison is the C_P taken at $\theta = 70$ degrees as shown in Figure 3d. These data indicate that the separation points are forward of $\theta = 70$ degrees and the steady flow data of Achenbach[5] for $2.6 < R_N \times 10^6 < 18.0$ indicate that the separation points in steady flow are located at $\theta \approx 40$ degrees. The pressure data presented herein indicate that in the separated flow regime, the data are reasonably comparable to the steady flow data; however, the location of the separation points or the gross flow structure is significantly different than the steady flow structure at corresponding Reynolds numbers. The comparison with potential theory indicates that ideal fluid calculations do not completely predict the flow fields about bluff bodies in unsteady flow.

FORCE MEASUREMENTS

Figure 4 and 5 present the instantaneous lift and drag coefficient data obtained for a time-dependent flow with an acceleration level of about 32 ft/sec^2. Again, these data represent the low frequency components, i.e., 0 to 20 Hz. A unique method of nondimensionalizing force data based on the same ideas reflected in the discussion of the pressure coefficient data was used in obtaining these results. For this application, the appropriate coefficient equation becomes

$$C_{l,(d)} = \frac{\text{Lift (Drag) Force/Length of Model}}{\left(1/2\, \rho_0\, U^2 + D\, \rho_0\, \frac{d\,U}{d\,t}\right) D} \qquad (2)$$

where D is the diameter of the cylinder and t is time. The data in Figure 5 indicate Reynolds number effects not unlike steady flow Reynolds number effects. The same sudden decrease in value at about a Reynolds number of 5×10^5 and the gradual increase thereafter is very apparent. Variation in the behavior of the instantaneous lift coefficient also occurs at about the same Reynolds number.

RESULTS AND CONCLUSIONS

Conclusions reached as a result of this research are:

1) Modification of the standard pressure coefficient definition to include Flow acceleration provides a useful tool in the understanding of time-dependent flows.

2) For the Reynolds number range of these tests, there are significant effects of viscosity noticeable through the Reynolds number on the unsteady pressure, force and flow visualization data.

3) The drag coefficient determined by integrating the pressure coefficient data compares favorably with that determined by the force measurement.

REFERENCES

1. NASA TM X-57779, "Meeting on Ground Wind Loads Problems in Relation to Launch Vehicles," Compilation of Papers Presented at the NASA Langley Research Center, June 7-8, 1966.

2. Schutzenhofer, L. A., "Development of an Unsteady Flow Apparatus and The Investigation of Unsteady Pressures on a Circular Cylinder in the Apparatus," M.S. Thesis, The University of Alabama, University, Alabama, 1969.

3. Morrow, D. J., "Experimental Investigation of the Unsteady Forces Imposed on a Submerged Circular Cylinder in Accelerating Flow," M.S. Thesis, The University of Alabama in Huntsville, Huntsville, Alabama, Unpublished.

4. Schlichting, H., Boundary Layer Theory, McGraw-Hill Book Co., Inc., New York, N. Y., Sixth Ed., 1968.

5. Achenbach, E., "Distribution of Local Pressure and Skin Friction Around a Circular Cylinder in Cross-Flow up to $R_e = 5 \times 10^6$," J. Fluid Mech., Vol. 34, Part 4, p. 625, 1968.

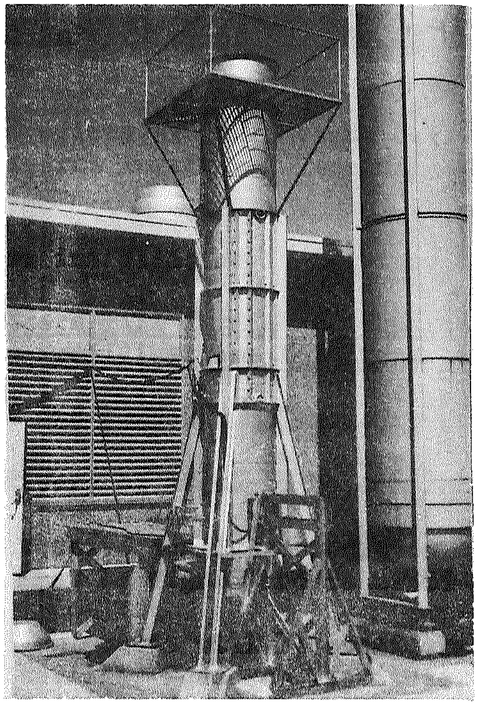

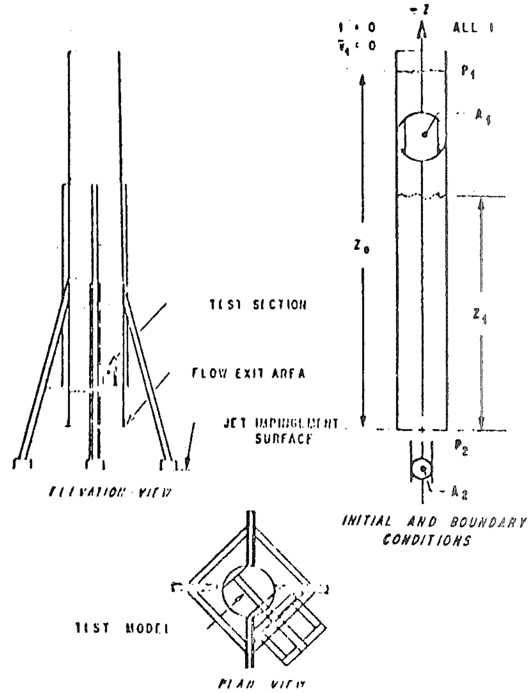

(a) (b)

FIGURE 1. GENERAL VIEW AND SCHEMATIC OF UNSTEADY TEST FACILITY

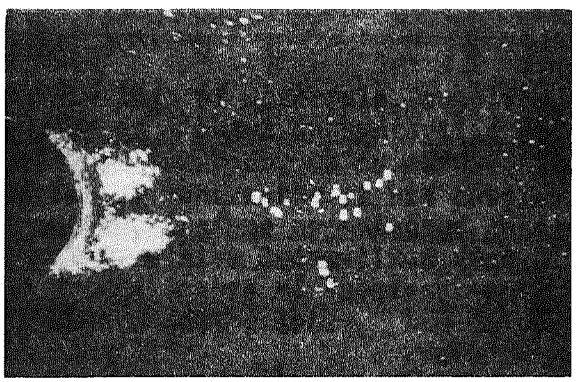

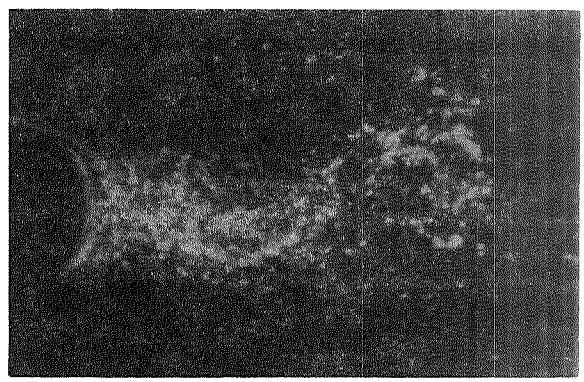

(a) (b)

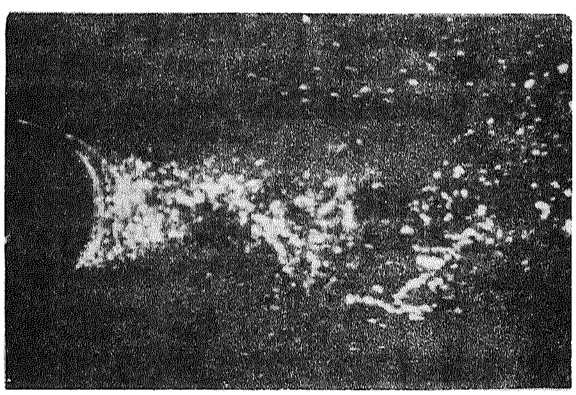

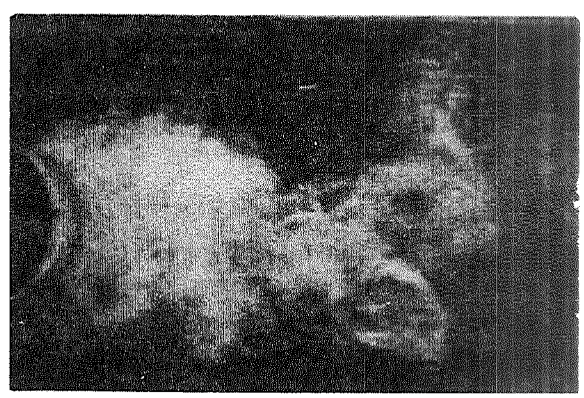

(c) (d)

FIGURE 2. PHOTOGRAPHIC SEQUENCE OF TYPICAL UNSTEADY FLOW FIELD

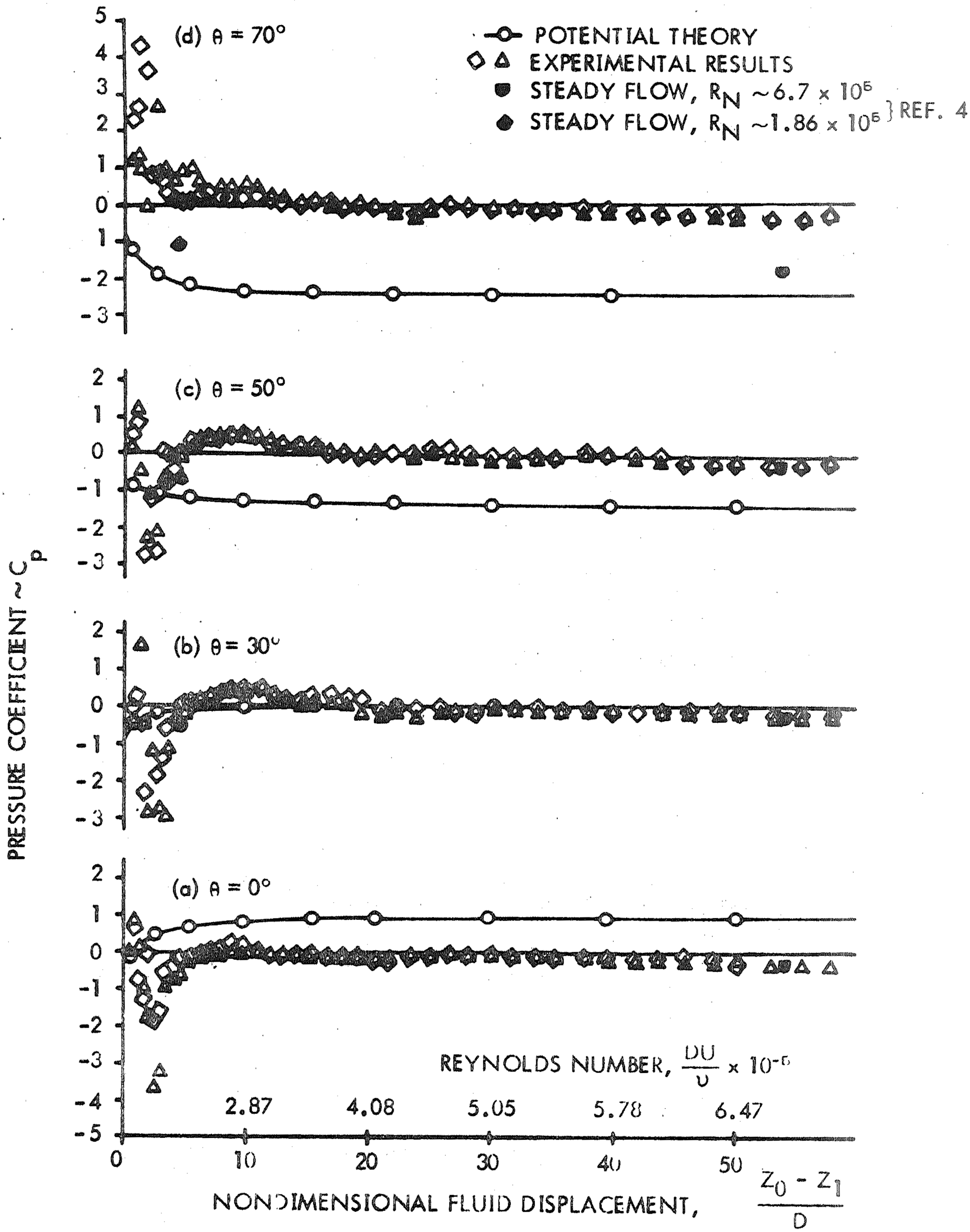

FIGURE 3. PRESSURE COEFFICIENT VERSUS NONDIMENSIONAL FLUID DISPLACEMENT FOR A CONSTANT ACCELERATION.

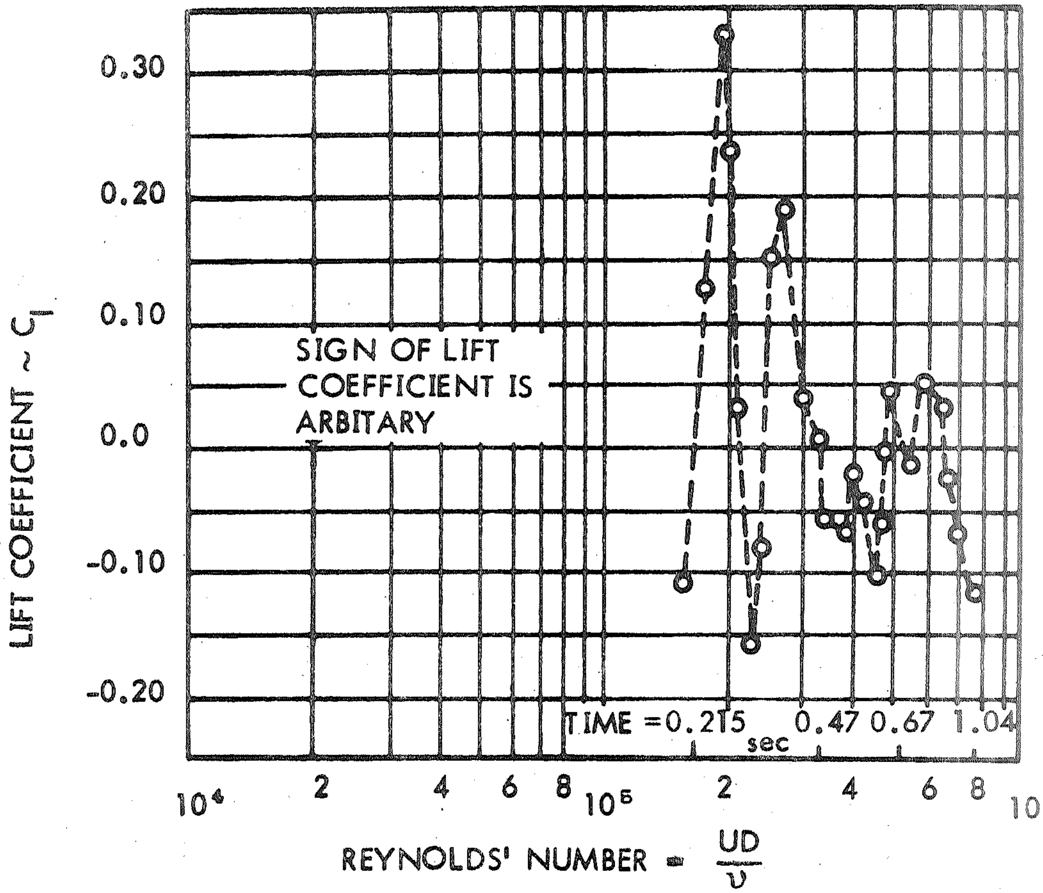

FIGURE 4 LIFT COEFFICIENT AS A FUNCTION OF REYNOLDS' NUMBER

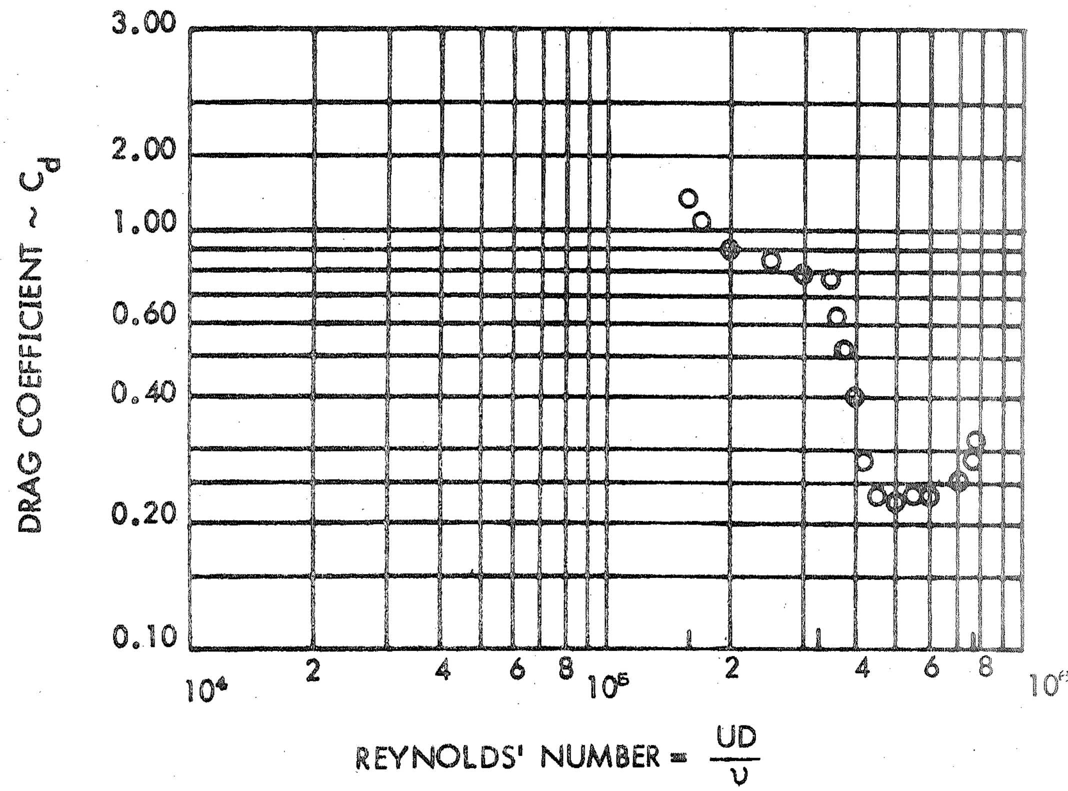

FIGURE 5. DRAG COEFFICIENT AS A FUNCTION OF REYNOLDS'

NUMBER